ACS APPLIED MATERIALS & INTERFACES

Research Article

Cite This: ACS Appl. Mater. Interfaces 2018, 10, 20559−20568

www.acsami.org

Exploring the Effect of Ligand-Originated MOF Isomerism and Methoxy Group Functionalization on Selective Acetylene/Methane and Carbon Dioxide/Methane Adsorption Properties in Two NbO-Type MOFs

Yao Wang,[†] Minghui He,[†] Xiaoxia Gao,[†] Saidan Li,[†] Shunshun Xiong,[‡] Rajamani Krishna,*[,§] and Yabing He*[,†]

[†]Key Laboratory of the Ministry of Education for Advanced Catalysis Materials, College of Chemistry and Life Sciences, Zhejiang Normal University, Jinhua 321004, China

[‡]Institute of Nuclear Physics and Chemistry, China Academy of Engineering Physics, Mianyang, Sichuan 621900, China

[§]Van't Hoff Institute for Molecular Sciences, University of Amsterdam, Science Park 904, 1098 XH Amsterdam, The Netherlands

Supporting Information

ABSTRACT: Investigation of the impact of ligand-originated MOF (metal−organic framework) isomerism and ligand functionalization on gas adsorption is of vital importance because a study in this aspect provides valuable guidance for future fabrication of new MOFs exhibiting better performance. For the abovementioned purpose, two NbO-type ligand-originated MOF isomers based on methoxy-functionalized diisophthalate ligands were solvothermally constructed in this work. Their gas adsorption properties toward acetylene, carbon dioxide, and methane were systematically investigated, revealing their promising potential for the adsorptive separation of both acetylene/methane and carbon dioxide/methane gas mixtures, which are involved in the industrial processes of acetylene production and natural gas sweetening. In particular, compared to its isomer **ZJNU-58**, **ZJNU-59** displays larger acetylene and carbon dioxide uptake capacities as well as higher acetylene/methane and carbon dioxide/methane adsorption selectivities despite its lower pore volume and surface area, demonstrating a very crucial role that the effect of pore size plays in acetylene and carbon dioxide adsorption. In addition, the impact of ligand modification with a methoxy group on gas adsorption was also evaluated. **ZJNU-58** exhibits slightly lower acetylene and carbon dioxide uptake capacities but higher acetylene/methane and carbon dioxide/methane adsorption selectivities as compared to its parent compound NOTT-103. By contrast, enhanced adsorption selectivities and uptake capacities were observed for **ZJNU-59** as compared to its parent compound **ZJNU-73**. The results demonstrated that the impact of ligand functionalization with a methoxy group on gas adsorption might vary from MOF to MOF, depending on the chosen parent compound. The results might shed some light on understanding the impact of both ligand-originated MOF isomerism and methoxy group functionalization on gas adsorption.

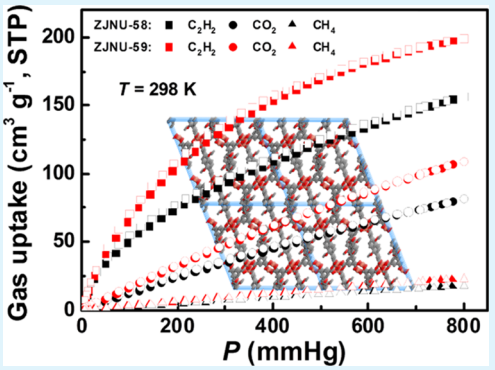

KEYWORDS: *metal−organic frameworks, ligand-originated isomerism, ligand functionalization, acetylene/methane separation, carbon dioxide/methane separation*

INTRODUCTION

Carbon dioxide/methane and acetylene/methane separations, which are involved in the industrial processes of natural gas sweetening and acetylene production, are two very important tasks in the chemical industry. Because the traditional cryogenic distillation is costly and less energy-efficient for the above-mentioned mixed-gas separation, considerable efforts have been devoted to developing porous materials capable of preferential adsorption of carbon dioxide and acetylene over methane at ambient conditions. Among various porous materials explored, porous metal−organic frameworks (MOFs) generated by coordinating assembly of multitopic organic ligands and metal ions/clusters have attracted continuous attention, presumably because they are highly chemically modulatable in terms of pore environment and pore/window size, which have been considered as two key parameters for gas separation. In principle, by altering both organic linkers and metal ions, the pore/window sizes can be precisely tuned to maximize the sieving effect, whereas their pore environment is capable of being decorated to direct the preferential recognition of target guests. Furthermore, by taking advantage of their crystalline structures, the gas adsorption mechanism including gas-binding

Received: March 31, 2018
Accepted: June 1, 2018
Published: June 1, 2018

DOI: 10.1021/acsami.8b05216
ACS Appl. Mater. Interfaces 2018, 10, 20559−20568

sites and host−guest interactions can be well comprehended through well-established diffraction techniques together with theoretical simulations, which, in turn, offers valuable information to rationally design new MOFs exhibiting improved performance. The abovementioned unique features make MOFs attractive candidates with vast promise for selective gas separation amongst other diverse potential applications.[1−5] In fact, a number of MOFs have been documented to display promising potential for carbon dioxide/methane and acetylene/methane separations.[6−13]

Since the first report in 2005,[14] NbO-type MOFs built up from linear diisophthalate ligands and dicopper paddle-wheel units have been increasingly studied for gas adsorption on account of their diverse surface-immobilizable functionalities, rich open copper sites, regulatable pore sizes, and moderately high surface area. For example, by varying the structural skeletons of the diisophthalate ligands and/or grafting different functional groups to the backbones of the diisophthalate ligands, Schröder et al. prepared a variety of linear diisophthalate ligands and constructed the associated NbO-type MOFs, exhibiting impressive hydrogen uptake capacities.[15] Afterward, other research groups have revealed that NbO-type MOFs also exhibit promising potential as methane and acetylene adsorbents.[16−24] In addition, NbO-type MOFs constitute an excellent platform for fundamental investigations of the structure−property relationship.[15,17,18,25] For instance, a comparative study of selective carbon dioxide adsorption in three NbO-type MOFs, whose diisophthalate ligands possess different orientations and numbers of nitrogen functional sites, was performed, demonstrating that the nitrogen accessibility degree has an important impact on selective carbon dioxide adsorption.[25] In light of these observations, we have been interested in exploring NbO-type MOFs for gas storage and separation for a long time.[18,19,21,24−31]

On the one hand, MOF polymorphism (also known as supramolecular isomerism) is ordinarily used to describe different network superstructures created by the same inorganic and organic building blocks and has become a very active subject in crystal engineering and supramolecular chemistry.[32−35] The research in this regard is of utmost significance because it helps us to understand the impact of the synthetic conditions on crystal growth and furthermore to deduce the structure−property relationship. However, rational design and controlled construction of such MOF isomers is exceedingly difficult. Comparatively, ligand-originated MOF isomerism might be synthetically controllable but remains less explored thus far.[36] Furthermore, the investigation of the impact of the ligand-originated MOF isomerism on the gas adsorption is also extremely limited. On the other hand, some previous research works have demonstrated that grafting specific functionalities into the organic linkers can improve the gas adsorption selectivity and uptake capacity of the resulting MOFs. Electron-donating functional groups such as amine group and nitrogen-containing heterocyclic rings have been frequently utilized to enhance carbon dioxide and acetylene uptakes considering that the carbon atom of carbon dioxide and the hydrogen atom of acetylene bring partial positive charges and thus are electron-accepting.[7,10,21,37−41] Comparatively, the impact of ligand functionalization with an alkoxy group on acetylene and carbon dioxide adsorption is limitedly known so far.

On the basis of the abovementioned considerations, we devised two diisophthalate ligands that are composed of two peripheral isophthalate units connected in distinct ways to the central naphthalene ring, which were deemed as a pair of positional isomers (Scheme 1). The positional isomerism originates from the interchanging of isophthalate moieties acting as coordinating sites and methoxy groups serving as functional groups. Solvothermal combination of these two diisophthalate ligands and copper ions resulted in the generation of two ligand-originated MOF isomers featuring the same NbO-type topology. Furthermore, their gas adsorption properties toward acetylene, carbon dioxide, and methane were systematically examined and compared in detail. Herein, we presented the solvothermal preparations, structural characterizations, and selective gas adsorption properties of the two resultant MOFs, with a particular focus on the exploration of the impact of ligand-originated MOF isomerism and ligand functionalization with a methoxy group on gas adsorption.

Scheme 1. Two Diisophthalate Positional Isomers (H_4L1 and H_4L2) Employed in This Work

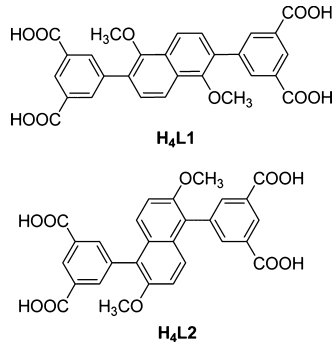

EXPERIMENTAL SECTION

General Remarks. Dimethyl 5-(4,4,5,5-tetramethyl-1,3,2-dioxaborolan-2-yl)isophthalate,[29] 2,6-dibromo-1,5-dimethoxynaphthalene,[42] and 1,5-dibromo-2,6-dimethoxynaphthalene[43] were synthesized according to the published literature. All other reagents were available from commercial sources and used as received without further treatment. The instruments used to record NMR (nuclear magnetic resonance) spectra, FTIR (Fourier transform infrared) spectra, the contents of C, H, and N, TGA (thermogravimetric analysis) profiles, PXRD (powder X-ray diffraction) patterns, gas isotherms, and single-crystal X-ray diffraction (SCXRD) data are, respectively, a Bruker AV400 or AV600 NMR spectrometer, a Nicolet 5DX FTIR spectrometer, a Vario EL III CHNOS elemental analyzer, a Netzsch STA 449C thermal analyzer, a Bruker D8 ADVANCE diffractometer, a Micromeritics ASAP 2020HD88 system, and a Bruker APEX II diffractometer. The detailed information can be found in the Supporting Information. CCDC nos. 1823336 and 1823337 contain the supplementary crystallographic data. The column breakthrough experiments were carried out according to our previously reported works.[10] Briefly, about 210 mg of activated **ZJNU-59** powder was packed into a stainless steel column (4 mm i.d./6.4 mm o.d. × 180 mm). The flow rates of the 50:50 (v/v) acetylene/methane and carbon dioxide/methane binary gas mixtures were maintained at 5 mL min^{-1}.

Synthesis and Characterization of 5,5′-(1,5-Dimethoxynaphthalene-2,6-diyl) Diisophthalic Acid (H_4L1). The synthesis procedure of H_4L1 was analogous to that in our previously published works.[44] Briefly, a mixture of 2,6-dibromo-1,5-dimethoxynaphthalene (1.00 g, 2.89 mmol), dimethyl 5-(4,4,5,5-tetramethyl-1,3,2-dioxaborolan-2-yl)isophthalate (2.06 g, 6.36 mmol), cesium carbonate (2.82 g, 8.67 mmol), and tetrakis(triphenylphosphine)palladium (0.17 g, 0.14 mmol) in 100 mL of anhydrous 1,4-dioxane was stirred at reflux under nitrogen for 72 h. After usual workup, the crude mixture was purified by recrystallization from toluene, affording the tetramethyl ester intermediate as a white solid in 49% yield (0.81 g, 1.41 mmol). The

DOI: 10.1021/acsami.8b05216
ACS Appl. Mater. Interfaces 2018, 10, 20559−20568

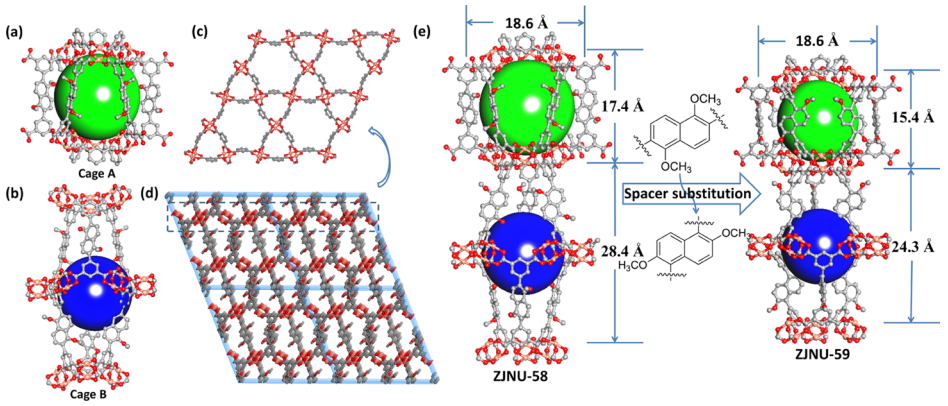

Figure 1. View of (a) cage A, (b) cage B, and (c) a 2D layer in **ZJNU-58**; (d) view of a 3D pillar-layered structure of **ZJNU-58**; and (e) a comparison of two distinct types of cages in **ZJNU-58** and **ZJNU-59**.

diisophthalate ligand H_4L1 was obtained by hydrolyzation of the tetramethyl ester intermediate with 20% sodium hydroxide aqueous solution (20 mL), followed by acidification with concentrated hydrochloric acid. The overall yield of the organic ligand H_4L1 is 48% (0.72 g, 1.39 mmol). For the tetramethyl ester intermediate, ^{1}H NMR ($CDCl_3$, 400.1 MHz): δ (ppm) 8.754 (t, J = 1.6 Hz, 2H), 8.628 (d, J = 1.6 Hz, 4H), 8.124 (d, J = 8.8 Hz, 2H), 7.621 (d, J = 8.8 Hz, 2H), 4.019 (s, 12H), 3.63 (s, 6H). For the acid, ^{1}H NMR (DMSO-d_6, 400.1 MHz): δ (ppm) 13.432 (s, 4H), 8.536 (t, J = 1.6 Hz, 2H), 8.482 (d, J = 1.6 Hz, 4H), 8.100 (d, J = 8.8 Hz, 2H), 7.741 (d, J = 8.8 Hz, 2H), 3.586 (s, 6H); ^{13}C NMR (DMSO-d_6, 150.0 MHz): δ (ppm) 167.018, 153.763, 138.866, 134.251, 132.170, 129.662, 129.428, 129.007, 128.775, 119.482, 62.026; selected FTIR (KBr, cm^{-1}): 1726, 1701, 1605, 1367, 1201, 1147, 1107, 1030, 962, 827, 756, 679, 669, 511.

Synthesis and Characterization of 5,5′-(2,6-Dimethoxynaphthalene-1,5-diyl) Diisophthalic Acid (H_4L2). The synthesis procedure of H_4L2 is similar to that of H_4L1 except that 2,6-dibromo-1,5-dimethoxynaphthalene is replaced by 1,5-dibromo-2,6-dimethoxynaphthalene. The overall yield of the organic ligand H_4L2 is 46%. For tetramethyl ester: ^{1}H NMR ($CDCl_3$, 400.1 MHz): δ (ppm) 8.799 (t, J = 1.6 Hz, 2H), 8.295 (d, J = 1.6 Hz, 4H), 7.453 (d, J = 8.8 Hz, 2H), 7.272 (d, J = 8.8 Hz, 2H), 3.987 (s, 12H), 3.796 (s, 6H). For acid, ^{1}H NMR (DMSO-d_6, 400.1 MHz): δ (ppm) 8.562 (t, J = 1.6 Hz, 2H), 8.079 (d, J = 1.6 Hz, 4H), 7.488 (d, J = 9.6 Hz, 2H), 7.389 (d, J = 9.6 Hz, 2H), 3.753 (s, 6H); ^{13}C NMR (DMSO-d_6, 160.9 MHz): 167.034, 152.475, 137.391, 136.109, 132.007, 129.383, 128.409, 126.492, 122.756, 115.705, 56.916; selected FTIR (KBr, cm^{-1}): 1695, 1593, 1512, 1452, 1389, 1259, 1066, 953, 922, 814, 760, 683, 611, 517.

Synthesis and Characterization of the MOF ZJNU-58. H_4L1 (5.0 mg, 9.7 μmol) and $CuCl_2{\cdot}2H_2O$ (10.0 mg, 58.7 μmol) were mixed in N,N'-dimethylformamide (DMF, 1.5 mL), methanol (0.5 mL), and water (0.1 mL) in a 20 mL scintillation vial. After 20 μL of 6 M HCl was added, the vial was sealed tightly and subsequently heated under static conditions at 343 K. After 24 h, the blue rhombic-shaped crystals thus produced were collected by filtration. The yield is about 41% based on the organic ligand H_4L1. As determined by the SCXRD structural determination together with TGA and microanalyses, the chemical formula for **ZJNU-58** can be best assigned to be $[Cu_2(L1)(H_2O)_2]{\cdot}6DMF{\cdot}CH_3OH{\cdot}H_2O$. Selected FTIR (KBr, cm^{-1}): 1655, 1437, 1363, 1255, 1101, 1038, 777, 727, 663, 492; Anal. Calcd for $C_{47}H_{68}N_6O_{20}Cu_2$: C, 48.49; H, 5.89; N, 7.22. Found: C, 48.38; H, 5.78; N, 7.24.

Synthesis and Characterization of the MOF ZJNU-59. H_4L2 (5.0 mg, 9.7 μmol) and $CuCl_2{\cdot}2H_2O$ (15.0 mg, 88.0 μmol) were mixed in DMF (1.5 mL) and water (0.2 mL) in a 20 mL scintillation vial. After 40 μL of 6 M HCl was added, the glass vial was sealed tightly and then placed at a preheated oven at 353 K at static conditions. After 72 h, the blue rhombic-shaped crystals thus formed were harvested. The yield is about 35% based on the organic ligand H_4L2. As determined by the SCXRD structural determination together with TGA and microanalyses, the chemical formula for **ZJNU-59** can be best assigned to be $[Cu_2(L2)(H_2O)_2]{\cdot}4DMF{\cdot}H_2O$. Selected FTIR (KBr, cm^{-1}): 1664, 1587, 1508, 1437, 1371, 1257, 1097, 1063, 775, 735, 712, 661, 615, 488; Anal. Calcd for $C_{40}H_{50}N_4O_{17}Cu_2$: C, 48.73; H, 5.11; N, 5.68. Found: C, 48.88; H, 5.13; N, 5.61.

RESULTS AND DISCUSSION

Synthesis and Characterization. The synthesis of the two diisophthalate ligands employed in this work could be accomplished in a two-step reaction in reasonable yields. Suzuki–Miyaura cross-coupling reaction between dimethyl 5-(4,4,5,5-tetramethyl-1,3,2-dioxaborolan-2-yl)isophthalate and 2,6-dibromo-1,5-dimethoxynaphthalene or 1,5-dibromo-2,6-dimethoxynaphthalene was carried out with tetrakis-(triphenylphosphine)palladium as a catalyst and cesium carbonate as a base. The tetramethyl ester intermediates thus formed were hydrolyzed and acidified to produce the corresponding diisophthalate ligands. All of the analytical data supported their chemical structures presented. Subsequently, a solvothermal reaction of these two ligands and copper ions afforded blue rhombic-shaped crystals, which were termed **ZJNU-58** (for H_4L1) and **ZJNU-59** (for H_4L2), respectively. Both **ZJNU-58** and **ZJNU-59** are not soluble in toluene, dichloromethane, acetonitrile, tetrahydrofuran, acetone, methanol, and DMF. The high similarities between the simulated and experimental PXRD patterns testified that the bulk materials of **ZJNU-58** and **ZJNU-59** have high phase purity (Figure S1). TGA showed a weight loss of 45.3% (calcd. 45.1% for 6DMF + MeOH + $3H_2O$) from ambient temperature to 535 K for **ZJNU-58** and a weight loss of 34.1% (calcd. 35.1% for 4DMF + $3H_2O$) from ambient temperature to 483 K for **ZJNU-59**, corresponding to the departure of both included solvents and binding aqua molecules (Figure S2). A comparison of the FTIR spectra of the two MOFs and their corresponding organic ligands indicated the full deprotonation of the organic ligands upon reacting with copper ions (Figure S3), which is in agreement with the SCXRD analyses mentioned below.

Structural Descriptions. SCXRD studies show that although **ZJNU-58** and **ZJNU-59** crystallize in different space groups ($C2/c$ for **ZJNU-58** and $R\bar{3}m$ for **ZJNU-59**), they are isoreticular. Therefore, we took **ZJNU-58** as a representative to describe the structure in the following section. **ZJNU-58** displays a 3D (three-dimensional) NbO-type network with unit cell parameters of a = 32.3534(9) Å, b = 18.2884(4) Å, c =

DOI: 10.1021/acsami.8b05216
ACS Appl. Mater. Interfaces 2018, 10, 20559–20568

32.7902(11) Å, and β = 111.698(4). Apart from the guest molecules, there are one and a half of completely deprotonated organic ligands, three independent copper ions (Cu1, Cu2, and Cu3), and three terminal aqua molecules in the asymmetric unit. Each copper ion exhibits a square-pyramidal $\{CuO_5\}$ coordination environment in which four carboxylate oxygen atoms coming from four different organic ligands and one oxygen atom belonging to the terminal aqua molecule are, respectively, located at the equatorial and axial positions. The distance of $Cu-O_{carboxylate}$ is 1.921−1.976 Å, which is in the range of the reported values for copper−polycarboxylate frameworks.[28,31,45,46] Comparatively, the $Cu-O_{water}$ distance is slightly longer because of Jahn−Teller effect, indicating that the terminal aqua molecule is readily removed. Bridging two neighboring copper ions with four carboxylate groups gave rise to the formation of a typical $Cu_2(COO)_4$ secondary building unit (SBU) with a Cu−Cu separation of 2.657−2.666 Å. Furthermore, the dicopper SBUs are linked together by the diisophthalate ligands to engender a 3D extended network architecture. The resulting framework incorporates two distinct types of cages. The spherical cage (cage A) consists of six organic ligands, six isophthalate moieties, and six $Cu_2(COO)_4$ units (Figure 1a), whereas the shuttle-shaped cage (cage B) is composed of six organic ligands and twelve $Cu_2(COO)_4$ units (Figure 1b). Both cage A and cage B have two distinct kinds of windows. The first kind of window is formed by interconnecting three isophthalate moieties with three $Cu_2(COO)_4$ units, whereas the second kind of window contains three $Cu_2(COO)_4$ units, which are bridged by two organic ligands and one isophthalate moiety. On the basis of the separation of the centroids of dicopper paddle-wheel units, the sizes are 9.145 × 0.245 × 9.338 Å for the first kind of window and 9.245 × 16.210 × 16.414 Å for the second kind of window. Alternatively, the framework of **ZJNU-58** can be regarded as a pillar-layered structure (Figure 1d). Concretely, the self-assembly of isophthalate moieties and $Cu_2(COO)_4$ units leads to the formation of the 2D (two-dimensional) layers (Figure 1c), while the backbones of the diisophthalate ligands function as pillars. As revealed by Platon calculations, the guest-accessible volume and the framework density of **ZJNU-58** are 65.1% and 0.7068 g cm^{-3}, respectively. For a better understanding of the structural differences between **ZJNU-58** and **ZJNU-59**, we analyzed and compared their two different types of cages (Figure 1e). It can be seen that the cages in **ZJNU-58** have the larger aspect ratio than the corresponding ones in **ZJNU-59**.

Pore Textural Properties. To obtain the desolvated MOFs for gas adsorption studies, the two MOFs were activated according to the following procedures. The guest molecules in as-made MOFs were exchanged with dry acetone, and the exchanged MOFs were then evacuated at 373 K until a degassed rate of 2 μm Hg min^{-1} was reached. During the activation, the color of the samples turned to dark blue from green, indicating the generation of open copper sites as a consequence of the removal of the terminal aqua molecules. Nitrogen (kinetic diameter: 3.64−3.80 Å) adsorption and desorption experiments at 77 K were carried out to evaluate the pore textural properties. The two MOFs displayed a reversible type-I adsorption behavior (Figure 2a), which is indicative of their microporous characteristics. The BET (Brunauer−Emmett−Teller) and Langmuir surface areas were estimated to be 2487 and 2738 m^2 g^{-1} for **ZJNU-58** and 2043 and 2188 m^2 g^{-1} for **ZJNU-59**, respectively, on the basis of the N_2 adsorption isotherms (Figures S4 and 5). In terms of the BET surface area, **ZJNU-58** surpasses or is comparable to some previously reported NbO-type MOFs such as UTSA-40 (1630 m^2 g^{-1}),[31] QI-Cu (1631 m^2 g^{-1}),[47] ZJNU-40 (2209 m^2 g^{-1}),[30] and NOTT-101 (2316 m^2 g^{-1}).[15] Compared to their parent compounds NOTT-103[48] and **ZJNU-73**,[36] **ZJNU-58** and **ZJNU-59** exhibit lower surface areas, which is due to the methoxy groups taking up part of their pore space. The higher surface area of **ZJNU-58** relative to **ZJNU-59** is attributed to the fact that the ligand used to construct the former is more elongated than that used to construct the latter. On the basis of the maximal values of N_2 adsorbed, the pore volumes of **ZJNU-58** and **ZJNU-59** were determined to be 0.976 and 0.781 cm^3 g^{-1}, respectively, which perfectly match the corresponding theoretical ones of 0.922 and 0.798 cm^3 g^{-1}, indicating high purity and full activation of the two MOFs.

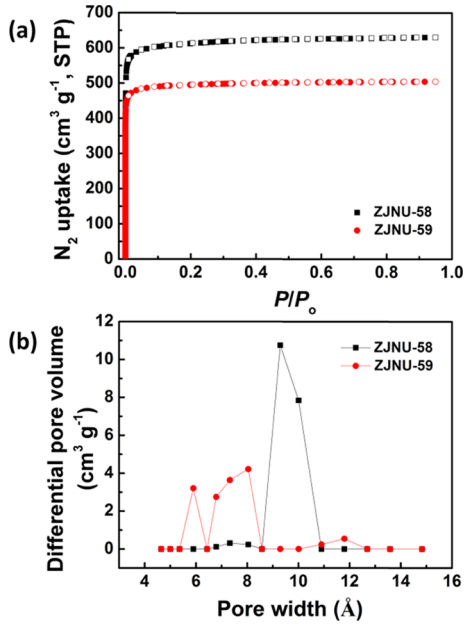

Figure 2. (a) N_2 adsorption (shown by the filled symbols) and desorption (shown by the open symbols) isotherms at 77 K and (b) density functional theory PSDs (pore size distributions) of **ZJNU-58** (black) and **ZJNU-59** (red).

Selective Adsorption of Carbon Dioxide and Acetylene from Methane. After the permanent porosity of **ZJNU-58** and **ZJNU-59** has been established by 77 K N_2 isotherms, we explored their potential application as adsorbents for the selective adsorption of acetylene and carbon dioxide from methane. Accordingly, pure-component acetylene, carbon dioxide, and methane isotherms were measured systematically at pressures up to 1.05 atm (106.6 kPa, 800 mm Hg) and three distinct temperatures (namely, 298, 288, and 278 K). As depicted in Figure 3, no hysteresis was observed for any isotherm, suggesting the completely reversible adsorption−desorption process. At 1.05 atm, the acetylene and carbon dioxide uptakes of **ZJNU-58** are 157.1 and 81.6 cm^3 (STP) g^{-1} at 298 K, 191.7 and 103.1 cm^3 (STP) g^{-1} at 288 K, and 228.5 and 129.5 cm^3 (STP) g^{-1} at 278 K, whereas the acetylene and carbon dioxide uptakes of **ZJNU-59** are 199.5 and 109.4 cm^3 (STP) g^{-1} at 298 K, 224.7 and 140.6 cm^3 (STP) g^{-1} at 288 K, and 248.1 and 178.3 cm^3 (STP) g^{-1} at 278 K, respectively. The acetylene uptake of **ZJNU-59** at ambient conditions exceeds those of some other porous materials[49−58] and is only

DOI: 10.1021/acsami.8b05216
ACS Appl. Mater. Interfaces 2018, 10, 20559−20568

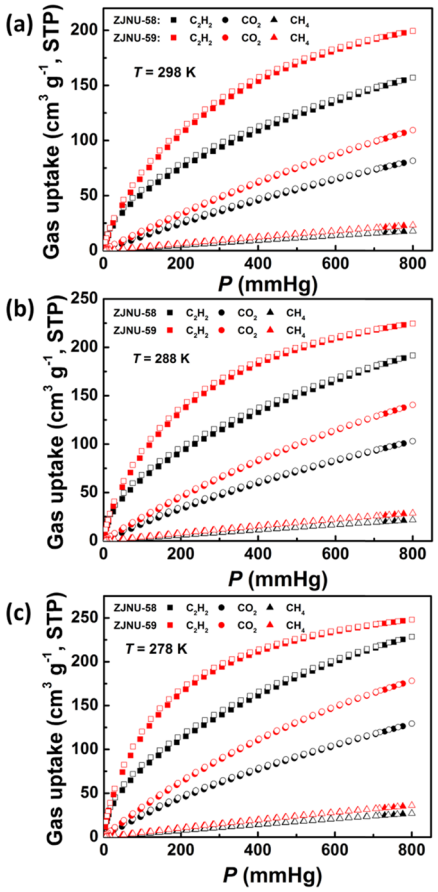

Figure 3. Acetylene, carbon dioxide, and methane adsorption (shown by the filled symbols) and desorption (shown by the open symbols) isotherms of **ZJNU-58** and **ZJNU-59** at (a) 298 K, (b) 288 K, and (c) 278 K.

surpassed by those of several top-performing MOFs such as MFM-188 (232 cm^3 (STP) g^{-1}),[59] FJI-H8 (224 cm^3 (STP) g^{-1}),[60] NJU-Bai17 (222.4 cm^3 (STP) g^{-1}),[20] and ZJNU-47 (213 cm^3 (STP) g^{-1}).[19] On the basis of the gravimetric acetylene uptake and the framework density, the acetylene storage density in the bulk material **ZJNU-59** is calculated to be 0.185 g cm^{-3} at 298 K and 1.05 atm, which is equivalent to the one at a hypothetical condition of 298 K and 17.6 MPa. The hypothetical pressure of 17.6 MPa is 88 times larger than an upper limiting pressure (0.2 MPa) for storing acetylene safely at room temperature. The carbon dioxide uptake of **ZJNU-59** at ambient conditions is comparable to and even exceeds the performance of some NbO-type MOFs explored for carbon dioxide capture, such as ZJNU-40 (108 cm^3 (STP) g^{-1}),[30] NJU-Bai14 (100 cm^3 (STP) g^{-1}),[61] NOTT-125 (92.59 cm^3 (STP) g^{-1}),[62] and SNU-50 (80 cm^3 (STP) g^{-1}).[63] Notably, despite its lower pore volume and surface area, **ZJNU-59** displays larger acetylene and carbon dioxide uptakes than its isomer **ZJNU-58**. Specifically, acetylene and carbon dioxide uptakes of **ZJNU-59** at 298 K and 1.05 atm are 27 and 34% higher than those of its isomer **ZJNU-58**, respectively. The result indicates a crucial role that the pore size effect plays in acetylene and carbon dioxide adsorption, considering that these two ligand-originated MOF isomers have the same chemical composition and gravimetric density of open copper sites (3.13 mmol g^{-1}). As determined by the N_2 adsorption isotherms (Figure 2b), **ZJNU-59** exhibits a pore width distribution at 5.4−8.6 Å, which is smaller than the corresponding value of 8.6−10.9 Å for **ZJNU-58**. As a result, the narrower pore size in **ZJNU-59** creates a higher van der Waals potential overlap and thus strengthens the interaction between gas molecules and the framework, offsetting the negative impact of the reduction of pore volume and surface area on gas adsorption. The enhanced gas−framework interactions have also been evidenced by the isosteric heat of gas adsorption (Q_{st}), which was extracted using the Clausius−Clapeyron equation from temperature-dependent isotherms. **ZJNU-58** and **ZJNU-59** have comparable Q_{st} values at the low coverage for carbon dioxide and acetylene adsorption. However, with the increasing gas loadings, the Q_{st} values for carbon dioxide and acetylene adsorption in **ZJNU-59** significantly exceed the corresponding ones in **ZJNU-58** (Figure S6).

In sharp contrast, the two MOFs exhibit very limited methane uptakes. The methane uptake of **ZJNU-58** at 1.05 atm is 17.9 cm^3 (STP) g^{-1} at 298 K, 21.7 cm^3 (STP) g^{-1} at 288 K, and 27.1 cm^3 (STP) g^{-1} at 278 K, whereas the methane uptake of **ZJNU-59** at 1.05 atm is 23.1 cm^3 (STP) g^{-1} at 298 K, 28.8 cm^3 (STP) g^{-1} at 288 K, and 36.1 cm^3 (STP) g^{-1} at 278 K. The significantly higher uptake capacities of acetylene and carbon dioxide relative to methane indicated their prospective application in the perspective of the preferential adsorption of carbon dioxide and acetylene over methane. To illustrate such a feasibility, we employed the well-established IAST (ideal adsorbed solution theory) to calculate the adsorption selectivity for the 50:50 (v/v) acetylene/methane and carbon dioxide/methane binary gas mixtures on the basis of the experimental pure-component isotherm data.[64] Figure 4 and Figures S9 and

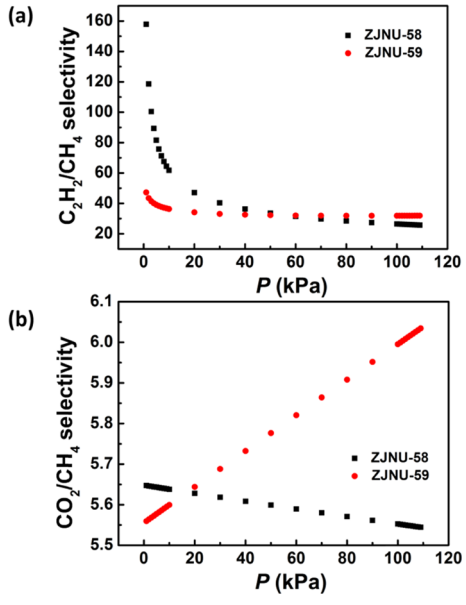

Figure 4. Comparison of (a) acetylene/methane and (b) carbon dioxide/methane IAST adsorption selectivities for the 50:50 (v/v) acetylene/methane and carbon dioxide/methane binary gas mixtures at 298 K in **ZJNU-58** and **ZJNU-59**.

10 in the Supporting Information present the predicted adsorption selectivities as a function of the bulk pressure. The acetylene/methane and carbon dioxide/methane adsorption selectivities in **ZJNU-58** at 1.05 atm are 25.7 and 5.5 at 298 K, which increase to 26.7 and 6.0 at 288 K and 28.0 and 6.6 at 278 K, respectively. For **ZJNU-59**, the acetylene/methane and

DOI: 10.1021/acsami.8b05216
ACS Appl. Mater. Interfaces 2018, 10, 20559−20568

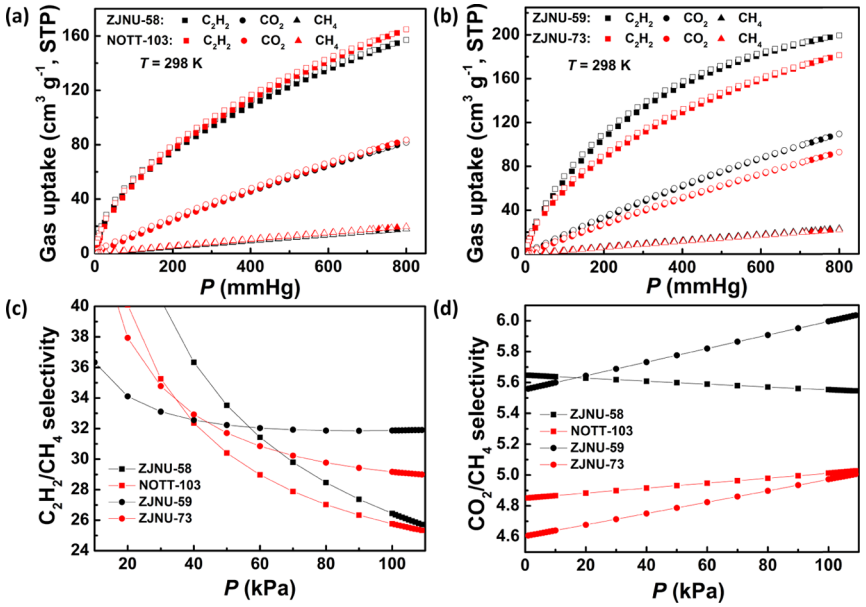

Figure 5. (a) Acetylene, carbon dioxide, and methane isotherms at 298 K of **ZJNU-58** and NOTT-103; (b) acetylene, carbon dioxide, and methane isotherms at 298 K of **ZJNU-59** and **ZJNU-73**; (c) comparison of acetylene/methane IAST adsorption selectivity for the 50:50 (v/v) acetylene/methane gas mixture at 298 K in **ZJNU-58**, **ZJNU-59**, NOTT-103, and **ZJNU-73**; and (d) comparison of carbon dioxide/methane IAST adsorption selectivity for the 50:50 (v/v) carbon dioxide/methane gas mixture at 298 K in **ZJNU-58**, **ZJNU-59**, NOTT-103, and **ZJNU-73**.

carbon dioxide/methane adsorption selectivities at 1.05 atm are 31.9 and 6.0 at 298 K, 38.4 and 6.9 at 288 K, and 47.3 and 7.9 at 278 K, respectively. In terms of the acetylene/methane IAST adsorption selectivity, **ZJNU-59** is superior to some previously reported MOFs such as $[InAg(na)_4]$ (17.3 at 273 K, na = nicotinic acid),[65] NOTT-101 (27.1),[18] ZJU-199 (27.3),[66] and ZJNU-71 (27.6).[67] In terms of the carbon dioxide/methane IAST adsorption selectivity, **ZJNU-59** is also comparable to and even surpasses some previously reported MOFs such as ZJNU-77 (5.7),[68] NOTT-101 (4.6),[30] and NJU-Bai20 (3.9).[69] The preferential adsorption of acetylene and carbon dioxide over methane in the two MOFs can be attributed to the structural feature of MOFs and the different physical properties between acetylene/carbon dioxide and methane molecules. The two MOFs incorporate open copper sites and methoxy functional groups, which are considered to be beneficial to enhance the affinity of the framework toward those easily polarized acetylene and carbon dioxide molecules. Besides, acetylene and carbon dioxide have higher critical temperatures than methane, meaning that they are easily condensable than methane. Noticeably, compared to its isomer **ZJNU-58**, **ZJNU-59** exhibits higher acetylene/methane and carbon dioxide/methane adsorption selectivities at 1.05 atm (Figure 4), following the same trend as the gas uptake capacities. Note that the uptake capacity and adsorption selectivity do not always go hand in hand in the reported MOFs.[2,70] Therefore, the higher adsorption selectivity and larger uptake capacity of **ZJNU-59** compared to its isomer **ZJNU-58** indicated its better performance for selective adsorption of acetylene and carbon dioxide from methane.

Next, to assess the impact of ligand functionalization with a methoxy group on gas adsorption, the gas adsorption isotherms of their parent compounds with respect to acetylene, carbon dioxide, and methane were measured at the same experimental conditions (Figure 5a,b). It should be mentioned that the parent MOF is NOTT-103[15] for **ZJNU-58** and **ZJNU-73**[36] for **ZJNU-59**. For NOTT-103, the acetylene and carbon dioxide uptakes at 1.05 atm are 164.8 and 83.5 cm^3 (STP) g^{-1} at 298 K, which increase to 207.0 and 106.5 cm^3 (STP) g^{-1} at 288 K and 254.9 and 134.6 cm^3 (STP) g^{-1} at 278 K, respectively. For **ZJNU-73**, the acetylene and carbon dioxide uptakes at 1.05 atm are 181.4 and 92.9 cm^3 (STP) g^{-1} at 298 K, 213.6 and 121.0 cm^3 (STP) g^{-1} at 288 K, and 246.3 and 156.9 cm^3 (STP) g^{-1} at 278 K, respectively. Analogously, the acetylene/methane and carbon dioxide/methane IAST adsorption selectivities were calculated to be 25.3 and 5.0 at 298 K, 27.8 and 5.5 at 288 K, and 31.5 and 6.1 at 278 K at 1.05 atm, respectively, in NOTT-103 for the 50:50 (v/v) acetylene/methane and carbon dioxide/methane binary gas mixtures (Figure 5c). The corresponding values are 29.0 and 5.0 at 298 K, 32.9 and 5.7 at 288 K, and 38.6 and 6.5 at 278 K at 1.05 atm in **ZJNU-73** (Figure 5d). Noticeably, **ZJNU-59** outperforms its parent compound **ZJNU-73** in terms of acetylene and carbon dioxide uptake capacities and acetylene/methane and carbon dioxide/methane adsorption selectivities at 298 K and 1.05 atm. By contrast, **ZJNU-58** shows slightly lower acetylene and carbon dioxide uptake capacities but higher acetylene/methane and carbon dioxide/methane adsorption selectivities as compared to its parent compound NOTT-103 under the same conditions. The results indicated that the impact of ligand functionalization with a methoxy group on gas adsorption might alter from MOF to MOF. In general, the introduction of the organic functional group into the parent framework will bring about the following two impacts: (1) the decrease of pore volume/surface area and (2) the reduction of pore size, which usually exert the opposite impact on the gas adsorption. Therefore, the enhanced gas uptake capacities of **ZJNU-59** compared to its parent compound **ZJNU-73** are mainly attributed to the effect of pore size reduction playing a domination role. In contrary, the decrease of pore volume and surface area upon the immobilization of methoxy groups should be responsible for the slightly inferior gas uptake capacity of **ZJNU-58** compared to its parent compound NOTT-103.

DOI: 10.1021/acsami.8b05216
ACS Appl. Mater. Interfaces 2018, 10, 20559−20568

To further compare the performances of **ZJNU-58**, **ZJNU-59**, and their parent compounds for the separation of acetylene/methane and carbon dioxide/methane gas mixtures, we performed transient breakthrough calculations (for the detailed information, see the Supporting Information). Figure 6a,b presents their breakthrough characteristics for the 50:50

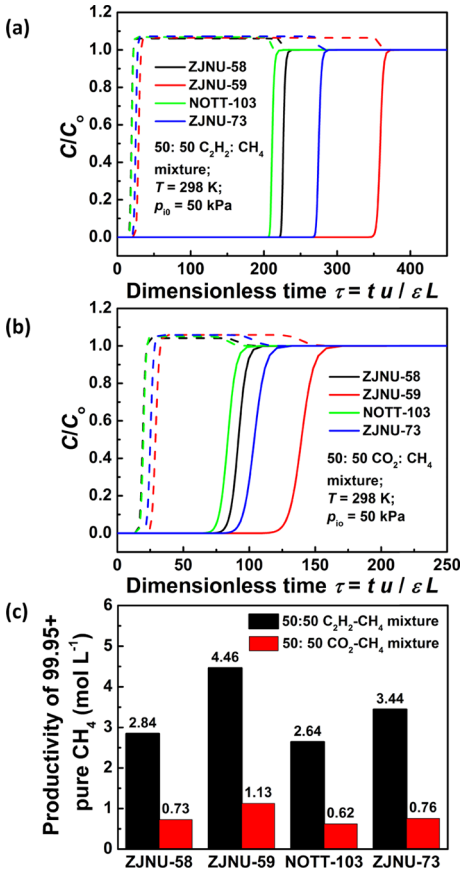

Figure 6. Transient breakthrough of (a) the 50:50 (v/v) acetylene (shown by the solid lines) and methane (shown by the dashed lines) mixtures and (b) the 50:50 (v/v) carbon dioxide (shown by the solid lines) and methane (shown by the dash lines) mixtures in four fixed bed adsorbers packed with **ZJNU-58**, **ZJNU-59**, NOTT-103, and **ZJNU-73**. (c) Comparison of the volumetric productivity of 99.95% + pure methane in **ZJNU-58**, **ZJNU-59**, NOTT-103, and **ZJNU-73**. In the breakthrough simulations, the total bulk gas phase is maintained at 298 K and 100 kPa.

(v/v) acetylene/methane and carbon dioxide/methane gas mixtures, which are operated at 298 K and 100 kPa (a total pressure). It can be observed that the breakthrough of acetylene and carbon dioxide happens at a significantly later time with **ZJNU-59**, suggesting that **ZJNU-59** has better performance for the separation of the two pairs of mixed gases. Also, the four different MOFs are compared in terms of the volumetric productivities of 99.95% + pure methane (Figure 6c). The highest productivity is achieved with **ZJNU-59** for the separation of the 50:50 (v/v) acetylene/methane and carbon dioxide/methane gas mixtures. The result is consistent with the above IAST calculations.

To validate the promising potential of **ZJNU-59** for the separation of acetylene/methane and carbon dioxide/methane gas mixtures, dynamic breakthrough experiments were also carried out. As depicted in Figure 7, acetylene and carbon

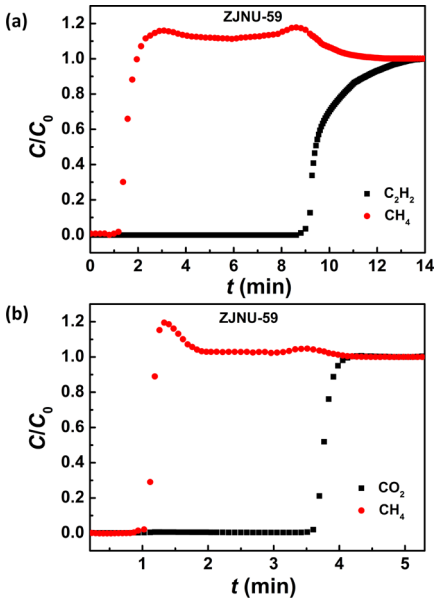

Figure 7. Experimental breakthrough curves for the 50:50 (v/v) (a) acetylene/methane and (b) carbon dioxide/methane gas mixtures at 298 K and 1 atm in **ZJNU-59**.

dioxide can be efficiently separated out from methane. On the basis of the breakthrough curves, the dynamic acetylene and carbon dioxide uptake capacities and the acetylene/methane and carbon dioxide/methane separation factors were calculated to be 5.26 and 2.02 mmol g^{-1} and 26.2 and 4.2, respectively.

CONCLUSIONS

Two ligand-originated MOF isomers with an underlying NbO-type topology were successfully solvothermally synthesized and structurally characterized. As established by single-component isotherm measurements combined with IAST calculations, the resultant two MOF compounds are the promising materials for selective adsorption of acetylene and carbon dioxide from methane. The impact of ligand-originated MOF isomerism on gas adsorption was explored. Compared to its isomer **ZJNU-58**, **ZJNU-59** exhibits larger acetylene and carbon dioxide uptake capacities as well as higher acetylene/methane and carbon dioxide/methane adsorption selectivities despite its lower pore volume and surface area, indicating its better performance for acetylene/methane and carbon dioxide/methane separations. By performing a comparative analysis of their structures and gas adsorption properties, it can be inferred that the more suitable pore size in **ZJNU-59** is responsible for its better performance. In addition, the impact of ligand modification with a methoxy group on gas adsorption was also investigated. **ZJNU-59** exhibits significantly enhanced acetylene and carbon dioxide uptake capacities compared to its parent compound **ZJNU-73**, whereas **ZJNU-58** displays acetylene and carbon dioxide uptake capacities slightly lower than those of its parent compound NOTT-103. However, enhanced acetylene/methane and carbon dioxide/methane adsorption selectivities were observed for these two MOFs when compared to their parent MOFs. The results demonstrated that the impact of ligand functionalization might vary from MOF to MOF, depending on the chosen parent compounds. This work not only reported two NbO-type MOFs for highly selective adsorption of acetylene and carbon dioxide from methane but also more importantly provided a basic understanding of the impact of

DOI: 10.1021/acsami.8b05216
ACS Appl. Mater. Interfaces 2018, 10, 20559−20568

both ligand-originated MOF isomerism and methoxy group functionalization on gas adsorption, which are very useful for the designed synthesis of new MOFs possessing better performance.

■ ASSOCIATED CONTENT

Supporting Information

The Supporting Information is available free of charge on the ACS Publications website at DOI: 10.1021/acsami.8b05216.

PXRD patterns; TGA curves; FTIR spectra; consistency, BET, and Langmuir plots; isosteric heat; isotherm fitting; IAST selectivities; N_2 isotherms and pore size distributions; NMR spectra; crystal data and structure refinement; Langmuir−Freundlich parameters (PDF)

Crystallographic data of **ZJNU-58** (CIF)

Crystallographic data of **ZJNU-59** (CIF)

■ AUTHOR INFORMATION

Corresponding Authors

*E-mail: r.krishna@contact.uva.nl (R.K.).

*E-mail: heyabing@zjnu.cn (Y.H.).

ORCID

Rajamani Krishna: 0000-0002-4784-8530

Yabing He: 0000-0002-0094-0591

Notes

The authors declare no competing financial interest.

■ ACKNOWLEDGMENTS

This research was financially supported by the Natural Science Foundation of Zhejiang province, China (LR16B010001), the National Natural Science Foundation of China (no. 21771162), and the Qianjiang Talents Project in Zhejiang province (ZC304015017).

■ REFERENCES

(1) Herm, Z. R.; Bloch, E. D.; Long, J. R. Hydrocarbon separations in metal-organic frameworks. *Chem. Mater.* **2014**, *26*, 323−338.

(2) He, Y.; Zhou, W.; Krishna, R.; Chen, B. Microporous metal-organic frameworks for storage and separation of small hydrocarbons. *Chem. Commun.* **2012**, *48*, 11813−11831.

(3) Wu, H.; Gong, Q.; Olson, D. H.; Li, J. Commensurate adsorption of hydrocarbons and alcohols in microporous metal organic frameworks. *Chem. Rev.* **2012**, *112*, 836−868.

(4) Ma, S.; Zhou, H.-C. Gas storage in porous metal-organic frameworks for clean energy applications. *Chem. Commun.* **2010**, *46*, 44−53.

(5) Li, J.-R.; Kuppler, R. J.; Zhou, H.-C. Selective gas adsorption and separation in metal-organic frameworks. *Chem. Soc. Rev.* **2009**, *38*, 1477−1504.

(6) Duan, X.; Zhou, Y.; Lv, R.; Yu, B.; Chen, H.; Jia, Z.; Cui, Y.; Yang, Y.; Qian, G. A new metal-organic framework for separation of C_2H_2/CH_4 and CO_2/CH_4 at room temperature. *J. Solid State Chem.* **2018**, *260*, 31−33.

(7) Jiao, J.; Jiang, D.; Chen, F.; Bai, D.; He, Y. A porous metal-organic framework based on an asymmetric angular diisophthalate for selective adsorption of C_2H_2 and CO_2 over CH_4. *Dalton Trans.* **2017**, *46*, 7813−7820.

(8) Guo, Z.-J.; Yu, J.; Zhang, Y.-Z.; Zhang, J.; Chen, Y.; Wu, Y.; Xie, L.-H.; Li, J.-R. Water-stable In(III)-based metal−organic frameworks with rod-shaped secondary building units: single-crystal to single-crystal transformation and selective sorption of C_2H_2 over CO_2 and CH_4. *Inorg. Chem.* **2017**, *56*, 2188−2197.

(9) Wang, L.; Ye, Y.; Li, Z.; Lin, Q.; Ouyang, J.; Liu, L.; Zhang, Z.; Xiang, S. Highly selective adsorption of C_2/C_1 mixtures and solven dependent thermochromic properties in metal-organic frameworks containing infinite copper-halogen chains. *Cryst. Growth Des.* **2017**, *17*, 2081−2089.

(10) Jiao, J.; Dou, L.; Liu, H.; Chen, F.; Bai, D.; Feng, Y.; Xiong, S.; Chen, D.-L.; He, Y. An aminopyrimidine-functionalized cage-based metal-organic framework exhibiting highly selective adsorption of C_2H_2 and CO_2 over CH_4. *Dalton Trans.* **2016**, *45*, 13373−13382.

(11) Zhang, Z.; Xiang, S.; Chen, Y.-S.; Ma, S.; Lee, Y.; Phely-Bobin, T.; Chen, B. A robust highly interpenetrated metal-organic framework constructed from pentanuclear clusters for selective sorption of gas molecules. *Inorg. Chem.* **2010**, *49*, 8444−8448.

(12) Procopio, E. Q.; Linares, F.; Montoro, C.; Colombo, V.; Maspero, A.; Barea, E.; Navarro, J. A. R. Cation-exchange porosity tuning in anionic metal-organic frameworks for the selective separation of gases and vapors and for catalysis. *Angew. Chem., Int. Ed.* **2010**, *49*, 7308−7311.

(13) Chen, Z.; Xiang, S.; Arman, H. D.; Li, P.; Tidrow, S.; Zhao, D.; Chen, B. A microporous metal-organic framework with immobilized -OH functional groups within the pore surfaces for selective gas sorption. *Eur. J. Inorg. Chem.* **2010**, *2010*, 3745−3749.

(14) Chen, B.; Ockwig, N. W.; Millward, A. R.; Contreras, D. S.; Yaghi, O. M. High H_2 adsorption in a microporous metal-organic framework with open metal sites. *Angew. Chem., Int. Ed.* **2005**, *44*, 4745−4749.

(15) Lin, X.; Telepeni, I.; Blake, A. J.; Dailly, A.; Brown, C. M.; Simmons, J. M.; Zoppi, M.; Walker, G. S.; Thomas, K. M.; Mays, T. J.; Hubberstey, P.; Champness, N. R.; Schröder, M. High capacity hydrogen adsorption in Cu(II) tetracarboxylate framework materials: the role of pore size, ligand functionalization, and exposed metal sites. *J. Am. Chem. Soc.* **2009**, *131*, 2159−2171.

(16) He, Y.; Chen, F.; Li, B.; Qian, G.; Zhou, W.; Chen, B. Porous metal organic frameworks for fuel storage. *Coord. Chem. Rev.* **2018**, DOI: 10.1016/j.ccr.2017.10.002.

(17) Zhang, M.; Zhou, W.; Pham, T.; Forrest, K. A.; Liu, W.; He, Y.; Wu, H.; Yildirim, T.; Chen, B.; Space, B.; Pan, Y.; Zaworotko, M. J.; Bai, J. Fine tuning of MOF-505 analogues to reduce low pressure methane uptake and enhance methane working capacity. *Angew. Chem., Int. Ed.* **2017**, *56*, 11426−11430.

(18) Chen, F.; Bai, D.; Wang, X.; He, Y. A comparative study of the effect of functional groups on C_2H_2 adsorption in NbO-Type Metal-Organic Frameworks. *Inorg. Chem. Front.* **2017**, *4*, 960−967.

(19) Song, C.; Jiao, J.; Lin, Q.; Liu, H.; He, Y. C_2H_2 adsorption in three isostructural metal-organic frameworks: boosting C_2H_2 uptake by rational arrangement of nitrogen sites. *Dalton Trans.* **2016**, *45*, 4563−4569.

(20) Zhang, M.; Li, B.; Li, Y.; Wang, Q.; Zhang, W.; Chen, B.; Li, S.; Pan, Y.; You, X.; Bai, J. Finely tuning MOFs towards high-performance in C_2H_2 storage: synthesis and properties of a new MOF-505 analogue with the inserted amide functional group. *Chem. Commun.* **2016**, *52*, 7241−7244.

(21) Song, C.; Hu, J.; Ling, Y.; Feng, Y.; Chen, D.-L.; He, Y. Merging open metal sites and Lewis basic sites in a NbO-type metal-organic framework for improved C_2H_2/CH_4 and CO_2/CH_4 separation. *Dalton Trans.* **2015**, *44*, 14823−14829.

(22) Li, B.; Wen, H.-M.; Wang, H.; Wu, H.; Tyagi, M.; Yildirim, T.; Zhou, W.; Chen, B. A porous metal-organic framework with dynamic pyrimidine groups exhibiting record high methane storage working capacity. *J. Am. Chem. Soc.* **2014**, *136*, 6207−6210.

(23) He, Y.; Zhou, W.; Qian, G.; Chen, B. Methane storage in metal-organic frameworks. *Chem. Soc. Rev.* **2014**, *43*, 5657−5678.

(24) He, Y.; Zhou, W.; Yildirim, T.; Chen, B. A series of metal-organic frameworks with high methane uptake and an empirical equation for predicting methane storage capacity. *Energy Environ. Sci.* **2013**, *6*, 2735−2744.

(25) Song, C.; Hu, J.; Ling, Y.; Feng, Y.; Krishna, R.; Chen, D.-l.; He, Y. The accessibility of nitrogen sites makes difference to selective CO_2 adsorption in a family of isostructural metal-organic frameworks. *J. Mater. Chem. A* **2015**, *3*, 19417−19426.

DOI: 10.1021/acsami.8b05216
ACS Appl. Mater. Interfaces 2018, 10, 20559−20568

(26) Song, C.; Liu, H.; Jiao, J.; Bai, D.; Zhou, W.; Yildirim, T.; He, Y. High methane storage and working capacities in a NbO-type metal-organic framework. *Dalton Trans.* **2016**, *45*, 7559−7562.
(27) Song, C.; Ling, Y.; Jin, L.; Zhang, M.; Chen, D.-L.; He, Y. CO_2 adsorption of three isostructural metal-organic frameworks depending on the incorporated highly polarized heterocyclic moieties. *Dalton Trans.* **2016**, *45*, 190−197.
(28) Jiao, J.; Liu, H.; Bai, D.; He, Y. A chemically cross-linked NbO-type metal-organic framework: cage or window partition? *Inorg. Chem.* **2016**, *55*, 3974−3979.
(29) Song, C.; Ling, Y.; Feng, Y.; Zhou, W.; Yildirim, T.; He, Y. A NbO-type metal-organic framework exhibiting high deliverable capacity for methane storage. *Chem. Commun.* **2015**, *51*, 8508−8511.
(30) Song, C.; He, Y.; Li, B.; Ling, Y.; Wang, H.; Feng, Y.; Krishna, R.; Chen, B. Enhanced CO_2 sorption and selectivity by functionalization of a NbO-type metal-organic framework with polarized benzothiadiazole moieties. *Chem. Commun.* **2014**, *50*, 12105−12108.
(31) He, Y.; Xiang, S.; Zhang, Z.; Xiong, S.; Wu, C.; Zhou, W.; Yildirim, T.; Krishna, R.; Chen, B. A microporous metal-organic framework assembled from an aromatic tetracarboxylate for H_2 purification. *J. Mater. Chem. A* **2013**, *1*, 2543−2551.
(32) Karmakar, A.; Paul, A.; Pombeiro, A. J. L. Recent advances on supramolecular isomerism in metal organic frameworks. *CrystEngComm* **2017**, *19*, 4666−4695.
(33) Zhang, J.-P.; Huang, X.-C.; Chen, X.-M. Supramolecular isomerism in coordination polymers. *Chem. Soc. Rev.* **2009**, *38*, 2385−2396.
(34) Makal, T. A.; Yakovenko, A. A.; Zhou, H.-C. Isomerism in metal-organic frameworks: "framework isomers". *J. Phys. Chem. Lett.* **2011**, *2*, 1682−1689.
(35) Moulton, B.; Zaworotko, M. J. From molecules to crystal engineering: supramolecular isomerism and polymorphism in network solids. *Chem. Rev.* **2001**, *101*, 1629−1658.
(36) Chen, F.; Bai, D.; Jiang, D.; Wang, Y.; He, Y. A comparative study of C_2H_2 adsorption properties in five isomeric copper-based MOFs based on naphthalene-derived diisophthalates. *Dalton Trans.* **2017**, *46*, 11469−11478.
(37) Liu, K.; Li, B.; Li, Y.; Li, X.; Yang, F.; Zeng, G.; Peng, Y.; Zhang, Z.; Li, G.; Shi, Z.; Feng, S.; Song, D. An N-rich metal-organic framework with an rht topology: high CO_2 and C_2 hydrocarbons uptake and selective capture from CH_4. *Chem. Commun.* **2014**, *50*, 5031−5033.
(38) Wang, X.-J.; Li, J.; Li, P.-Z.; Xing, L.-B.; Lu, H.; Wu, H.; Shi, Y.; Zou, R.; Zhao, Y. An amine functionalized *rht*-type metal-organic framework with the improved performance for gas uptake. *Inorg. Chem. Commun.* **2014**, *46*, 13−16.
(39) Wang, X.-J.; Li, P.-Z.; Chen, Y.; Zhang, Q.; Zhang, H.; Chan, X. X.; Ganguly, R.; Li, Y.; Jiang, J.; Zhao, Y. A rationally designed nitrogen-rich metal-organic framework and its exceptionally high CO_2 and H_2 uptake capability. *Sci. Rep.* **2013**, *3*, 1149.
(40) Lin, Q.; Wu, T.; Zheng, S.-T.; Bu, X.; Feng, P. Single-walled polytetrazolate metal-organic channels with high density of open nitrogen-donor sites and gas uptake. *J. Am. Chem. Soc.* **2012**, *134*, 784−787.
(41) Vaidhyanathan, R.; Iremonger, S. S.; Shimizu, G. K. H.; Boyd, P. G.; Alavi, S.; Woo, T. K. Direct observation and quantification of CO_2 binding within an amine-functionalized nanoporous solid. *Science* **2010**, *330*, 650−653.
(42) Alvey, P. M.; Ono, R. J.; Bielawski, C. W.; Iverson, B. L. Conjugated NDI−donor polymers: exploration of donor size and electrostatic complementarity. *Macromolecules* **2013**, *46*, 718−726.
(43) Wang, J.-Y.; Zhou, Y.; Yan, J.; Ding, L.; Ma, Y.; Cao, Y.; Wang, J.; Pei, J. New fused heteroarenes for high-performance field-effect transistors. *Chem. Mater.* **2009**, *21*, 2595−2597.
(44) Wang, Y.; He, M.; Tian, Z.; Zhong, H.; Zhu, L.; Zhang, Y.; Zhang, X.; Chen, D.-L.; He, Y. Rational construction of a *ssa*-Type of MOF through preorganizing the ligand's conformation and its exceptional gas adsorption properties. *Dalton Trans.* **2018**, *47*, 2444−2452.
(45) He, Y.; Guo, Z.; Xiang, S.; Zhang, Z.; Zhou, W.; Fronczek, F. R.; Parkin, S.; Hyde, S. T.; O'Keeffe, M.; Chen, B. Metastable interwoven mesoporous metal-organic frameworks. *Inorg. Chem.* **2013**, *52*, 11580−11584.
(46) He, Y.; Zhang, Z.; Xiang, S.; Wu, H.; Fronczek, F. R.; Zhou, W.; Krishna, R.; O'Keeffe, M.; Chen, B. High separation capacity and selectivity of C_2 hydrocarbons over methane within a microporous metal-organic framework at room temperature. *Chem.—Eur. J.* **2012**, *18*, 1901−1904.
(47) Wang, C.; Li, L.; Tang, S.; Zhao, X. Enhanced uptake and selectivity of CO_2 adsorption in a hydrostable metal-organic frameworks via incorporating methylol and methyl groups. *ACS Appl. Mater. Interfaces* **2014**, *6*, 16932−16940.
(48) Lin, X.; Jia, J.; Zhao, X.; Thomas, K. M.; Blake, A. J.; Walker, G. S.; Champness, N. R.; Hubberstey, P.; Schröder, M. High H_2 adsorption by coordination-framework materials. *Angew. Chem., Int. Ed.* **2006**, *45*, 7358−7364.
(49) Chen, D.-M.; Zhang, N.-N.; Tian, J.-Y.; Liu, C.-S.; Du, M. Pore modulation of metal-organic frameworks towards enhanced hydrothermal stability and acetylene uptake via incorporating different functional brackets. *J. Mater. Chem. A* **2017**, *5*, 4861−4867.
(50) Yan, Y.; Juríček, M.; Coudert, F.-X.; Vermeulen, N. A.; Grunder, S.; Dailly, A.; Lewis, W.; Blake, A. J.; Stoddart, J. F.; Schröder, M. Non-interpenetrated metal-organic frameworks based on copper(II) paddlewheel and oligoparaxylene-isophthalate linkers: synthesis, structure, and gas adsorption. *J. Am. Chem. Soc.* **2016**, *138*, 3371−3381.
(51) Zhou, L.-J.; Deng, W.-H.; Wang, Y.-L.; Xu, G.; Yin, S.-G.; Liu, Q.-Y. Lanthanide−potassium biphenyl-3,3′-disulfonyl-4,4′-dicarboxylate frameworks: gas sorption, proton conductivity, and luminescent sensing of metal ions. *Inorg. Chem.* **2016**, *55*, 6271−6277.
(52) Chen, D.-M.; Tian, J.-Y.; Liu, C.-S. Ligand symmetry modulation for designing mixed-ligand metal-organic frameworks: gas sorption and luminescence sensing properties. *Inorg. Chem.* **2016**, *55*, 8892−8897.
(53) Liu, K.; Li, B.; Li, Y.; Li, X.; Yang, F.; Zeng, G.; Peng, Y.; Zhang, Z.; Li, G.; Shi, Z.; Feng, S.; Song, D. N-rich metal-organic framework with *rht* topology: high CO_2 and C_2 hydrocarbons uptake and selective capture from CH_4. *Chem. Commun.* **2014**, *50*, 5031−5033.
(54) Lee, S.-J.; Yoon, J. W.; Seo, Y.-K.; Kim, M.-B.; Lee, S.-K.; Lee, U.-H.; Hwang, Y. K.; Bae, Y.-S.; Chang, J.-S. Effect of purification conditions on gas storage and separations in a chromium-based metal-organic framework MIL-101. *Microporous Mesoporous Mater.* **2014**, *193*, 160−165.
(55) Yang, S.; Ramirez-Cuesta, A. J.; Newby, R.; Garcia-Sakai, V.; Manuel, P.; Callear, S. K.; Campbell, S. I.; Tang, C. C.; Schröder, M. Supramolecular binding and separation of hydrocarbons within a functionalized porous metal-organic framework. *Nat. Chem.* **2015**, *7*, 121−129.
(56) He, Y.; Xiang, S.; Chen, B. A microporous hydrogen-bonded organic framework for highly selective C_2H_2/C_2H_4 separation at ambient temperature. *J. Am. Chem. Soc.* **2011**, *133*, 14570−14573.
(57) Tanaka, D.; Higuchi, M.; Horike, S.; Matsuda, R.; Kinoshita, Y.; Yanai, N.; Kitagawa, S. Storage and sorption properties of acetylene in jungle-gym-like open frameworks. *Chem.—Asian J.* **2008**, *3*, 1343−1349.
(58) Matsuda, R.; Kitaura, R.; Kitagawa, S.; Kubota, Y.; Belosludov, R. V.; Kobayashi, T. C.; Sakamoto, H.; Chiba, T.; Takata, M.; Kawazoe, Y.; Mita, Y. Highly controlled acetylene accommodation in a metal-organic microporous material. *Nature* **2005**, *436*, 238−241.
(59) Moreau, F.; Silva, I. d.; Smail, N. H. A.; Easun, T. L.; Savage, M.; Godfrey, H. G. W.; Parker, S. F.; Manuel, P.; Yang, S.; Schröder, M. Unravelling exceptional acetylene and carbon dioxide adsorption within a tetra-amide functionalized metal-organic framework. *Nat. Commun.* **2016**, *8*, 14085.
(60) Pang, J.; Jiang, F.; Wu, M.; Liu, C.; Su, K.; Lu, W.; Yuan, D.; Hong, M. A porous metal-organic framework with ultrahigh acetylene uptake capacity under ambient conditions. *Nat. Commun.* **2015**, *6*, 7575.

DOI: 10.1021/acsami.8b05216
ACS Appl. Mater. Interfaces 2018, 10, 20559−20568

(61) Zhang, M.; Wang, Q.; Lu, Z.; Liu, H.; Liu, W.; Bai, J. A nitro-decorated NbO-type metal-organic framework with highly selective CO_2 uptake and CH_4 storage capacity. *CrystEngComm* **2014**, *16*, 6287−6290.
(62) Alsmail, N. H.; Suyetin, M.; Yan, Y.; Cabot, R.; Krap, C. P.; Lü, J.; Easun, T. L.; Bichoutskaia, E.; Lewis, W.; Blake, A. J.; Schröder, M. Analysis of high and selective uptake of CO_2 in an oxamide-containing $\{Cu_2(OOCR)_4\}$-based metal-organic framework. *Chem.—Eur. J.* **2014**, *20*, 7317−7324.
(63) Prasad, T. K.; Hong, D. H.; Suh, M. P. High gas sorption and metal-ion exchange of microporous metal-organic frameworks with incorporated imide Groups. *Chem.—Eur. J.* **2010**, *16*, 14043−14050.
(64) Myers, A. L.; Prausnitz, J. M. Thermodynamics of mixed-gas adsorption. *AIChE J.* **1965**, *11*, 121−127.
(65) Tan, Y.-X.; He, Y.-P.; Zhang, J. High and selective sorption of C_2 hydrocarbons in heterometal-organic frameworks built from tetrahedral units. *RSC Adv.* **2015**, *5*, 7794−7797.
(66) Zhang, L.; Zou, C.; Zhao, M.; Jiang, K.; Lin, R.; He, Y.; Wu, C.-D.; Cui, Y.; Chen, B.; Qian, G. Doubly interpenetrated metal-organic framework for highly selective C_2H_2/CH_4 and C_2H_2/CO_2 separation at room temperature. *Cryst. Growth Des.* **2016**, *16*, 7194−7197.
(67) Chen, F.; Wang, Y.; Bai, D.; He, M.; Gao, X.; He, Y. Selective adsorption of C_2H_2 and CO_2 from CH_4 in an isoreticular series of MOFs constructed from unsymmetrical diisophthalate linkers and the effect of alkoxy group functionalization on gas adsorption. *J. Mater. Chem. A* **2018**, *6*, 3471−3478.
(68) Chen, F.; Bai, D.; Wang, Y.; He, M.; Gao, X.; He, Y. A pair of polymorphous metal-organic frameworks based on an angular diisophthalate linker: synthesis, characterization and gas adsorption properties. *Dalton Trans.* **2018**, *47*, 716−725.
(69) Lu, Z.; Bai, J.; Hang, C.; Meng, F.; Liu, W.; Pan, Y.; You, X. The utilization of amide groups to expand and functionalize metal-organic frameworks simultaneously. *Chem.—Eur. J.* **2016**, *22*, 6277−6285.
(70) He, Y.; Krishna, R.; Chen, B. Metal-organic frameworks with potential for energy-efficient adsorptive separation of light hydrocarbons. *Energy Environ. Sci.* **2012**, *5*, 9107−9120.

DOI: 10.1021/acsami.8b05216
ACS Appl. Mater. Interfaces 2018, 10, 20559−20568

Supporting Information

Exploring the Effect of Ligand-Originated MOF Isomerism and Methoxy Group Functionalization on Selective Acetylene/Methane and Carbon Dioxide/Methane Adsorption Properties in Two NbO-Type MOFs

Yao Wang,† Minghui He,† Xiaoxia Gao,† Saidan Li,† Shunshun Xiong,‡ Rajamani Krishna*‖ and Yabing He*†

† Key Laboratory of the Ministry of Education for Advanced Catalysis Materials, College of Chemistry and Life Sciences, Zhejiang Normal University, Jinhua 321004, China. E-mail: heyabing@zjnu.cn

‡ Institute of Nuclear Physics and Chemistry, China Academy of Engineering Physics, Mianyang, Sichuan 621900, China

‖ Van ‘t Hoff Institute for Molecular Sciences, University of Amsterdam, Science Park 904, 1098 XH Amsterdam, The Netherlands. E-mail: r.krishna@contact.uva.nl

General remarks. ^{1}H and ^{13}C NMR (Nuclear Magnetic Resonance) spectra were measured on a Bruker AV400 or AV600 NMR spectrometer. Chemical shifts (δ) were reported in ppm (parts per million) relative to the proton or carbon resonances of the residual undeuterated solvents ($CDCl_3$: δ = 7.26 ppm for ^{1}H NMR and δ = 77.1 ppm for ^{13}C NMR; DMSO-d_6: δ = 2.50 ppm for ^{1}H NMR and δ = 39.5 ppm for ^{13}C NMR), and coupling constants (J) were reported in Hertz (Hz). Abbreviations for signal couplings are as follows: s, singlet; d, doublet; t, triplet; q, quartet; m, multiplet; br, broad. FTIR (Fourier Transform Infrared) spectra were taken on KBr pellets in the range of 4000-400 cm^{-1} using a Nicolet 5DX FTIR spectrometer. Elemental analyses (C, H, and N) were performed using a Vario EL III CHNOS elemental analyzer. TGA (Thermogravimetric Analyses) were performed on a Netzsch STA 449C thermal analyzer with a heating rate of 5 K min^{-1} under a nitrogen stream. PXRD (Powder X-ray Diffraction) experiments were carried out in a reflection mode using a Bruker D8 Advance diffractometer equipped with a Cu-sealed tube at 40 kV and 40 mA (λ = 1.5406 Å) over a 2θ range of 5-45^{o} at room temperature, and MOF materials were ground to a fine powder prior to PXRD measurements. Simulated PXRD patterns were derived from the single-crystal X-ray diffraction data by utilizing the Mercury software (version 1.4.1). Gas adsorption desorption isotherms were recorded using a Micromeritics ASAP 2020HD88 system. High-purity gases (N_2, 99.9999%; C_2H_2, 99.9%; CO_2, 99.999%; CH_4, 99.99%) were used for the adsorption measurements. The samples were maintained at 77 K by immersing the sample tube in a liquid-nitrogen bath, and at other temperatures by using a circulating water bath (Julabo F12ED). The column breakthrough experiments were carried out according to our previously reported procedures.[1] About 210 mg of activated **ZJNU-59** powder was packed into a stainless steel column (4 mm I.D. / 6.4 mm O.D. × 180 mm) with silica wool filling the void space. Two gas mixtures, namely, C_2H_2–CH_4 (50: 50, *v*/*v*) and CO_2-CH_4 (50: 50, *v*/*v*), were allowed to flow into the column at a rate of 5 mL min^{-1}.

Crystal structure determinations. Single-crystal X-ray crystal data collection was carried out using a Bruker APEX II diffractometer with graphite monochromated

Mo-K_a (λ = 0.71073 Å) or Cu-K_a (λ = 1.54184 Å) radiation. The structures were solved by direct methods and refined with the full-matrix least-squares on F^2 using the SHELXT-97 program package. Non-hydrogen atoms were refined with anisotropic displacement parameters during final cycles. Hydrogen atoms were placed in geometrically idealized positions and refined using a riding model. The SQUEEZE subroutine of the PLATON software suite was employed to remove the scattering from the disordered guest molecules. The resulting new *HKL* files were used to further refine the structures. The crystal data and refinement parameters were listed in Table S1. CCDC No. 1823336 and 1823337 contain the supplementary crystallographic data for this paper.

Gas isotherm fitting

The pure-component C_2H_2, CO_2 and CH_4 adsorption isotherms measured at 278 K, 288 K, and 298 K were fitted with the single-site Langmuir-Freundlich model

$$q = \frac{q_{sat} b p^{v}}{1 + b p^{v}}, \text{ with } T\text{-dependent parameter } \quad b = b_o \exp(\frac{E_a}{RT})$$

where q is the adsorbed amount (mmol g^{-1}), q_{sat} is the monolayer adsorption capacity (mmol g^{-1}), p is the equilibrium pressure (kPa), and b and v is the Langmuir and Freundlich constants. The corresponding fitting parameters are provided in Tables S2-S5. Fig S7 provides a comparison of the experimental isotherm data for C_2H_2, CO_2, and CH_4 in **ZJNU-58** with the isotherm fits. Fig S8 provides a comparison of the experimental isotherm data for C_2H_2, CO_2, and CH_4 in **ZJNU-59** with the isotherm fits. Fig S15 provides a comparison of the experimental isotherm data for C_2H_2, CO_2, and CH_4 in **NOTT-103** with the isotherm fits. Fig S16 provides a comparison of the experimental isotherm data for C_2H_2, CO_2, and CH_4 in **ZJNU-73** with the isotherm fits.

Q_{st} calculations

The isosteric heats of adsorption (Q_{st}) were calculated using the Clausius-Clapeyron equation based on pure-component isotherms collected at three different temperatures of 278 K, 288 K, and 298 K. The Q_{st} was defined as

$$Q_{st} = -R\left(\frac{\partial Inp}{\partial(1/T)}\right)_q$$

where p is the pressure, T is the temperature, R is the gas constant, and q is the adsorption amount. These calculations were done through the "Heat of Adsorption" function embedded in the software supplied by Micromeritics ASAP 2020HD88 surface-area-and-pore-size analyzer machine.

IAST calculations

The selectivity of preferential adsorption of component 1 over component 2 in a mixture containing 1 and 2 can be formally defined as

$$S_{ads} = \frac{q_1/q_2}{p_1/p_2}$$

where q_1 and q_2 are the component loadings of the adsorbed phase in the mixture. These component loadings are also termed the uptake capacities. We calculate the values of q_1 and q_2 using the Ideal Adsorbed Solution Theory (IAST) of Myers and Prausnitz.

Transient breakthrough calculations

The performance of industrial fixed bed adsorbers is dictated by a combination of adsorption selectivity and uptake capacity. For a proper evaluation of MOFs, we performed transient breakthrough simulations using the simulation methodology described in the literature.[2-5] For the breakthrough simulations, the following parameter values were used: length of packed bed, L = 0.3 m; voidage of packed bed, ε = 0.4; superficial gas velocity at inlet, u = 0.04 m s^{-1}. The transient breakthrough simulation results are presented in terms of a *dimensionless* time, τ, defined by dividing the actual time, t, by the characteristic time, $\frac{L\varepsilon}{u}$.

In the breakthrough simulations with the four MOFs, the total bulk gas phase is at 298 K and 100 kPa. For C_2H_2/CH_4 mixtures, the inlet partial pressures are 50 kPa for each component. From a material balance, the productivity of 99.95%+ pure CH_4 can be determined. The highest productivity is achieved with **ZJNU-59**. For CO_2/CH_4 mixtures, the inlet partial pressures are 50 kPa for each component. From a material

balance, the productivity of 99.95%+ pure CH_4 can be determined. The highest productivity is achieved with **ZJNU-59**.

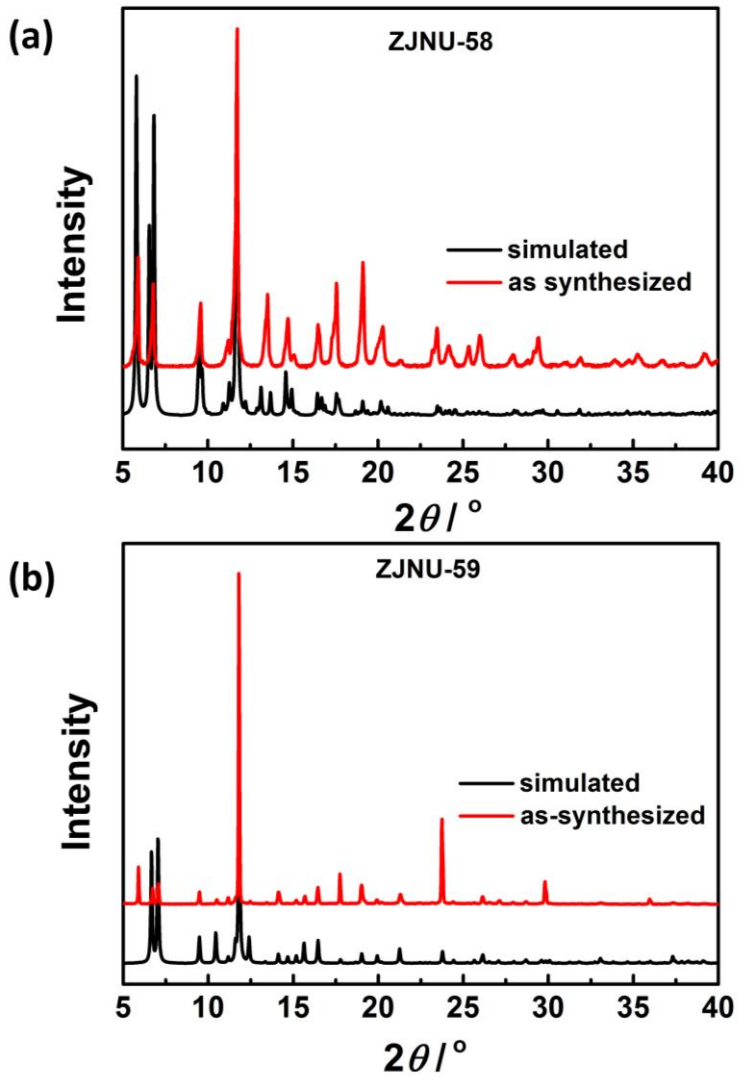

Figure S1. Comparison of the experimental (red) and simulated (black) PXRD patterns for (a) **ZJNU-58** and (b) **ZJNU-59**.

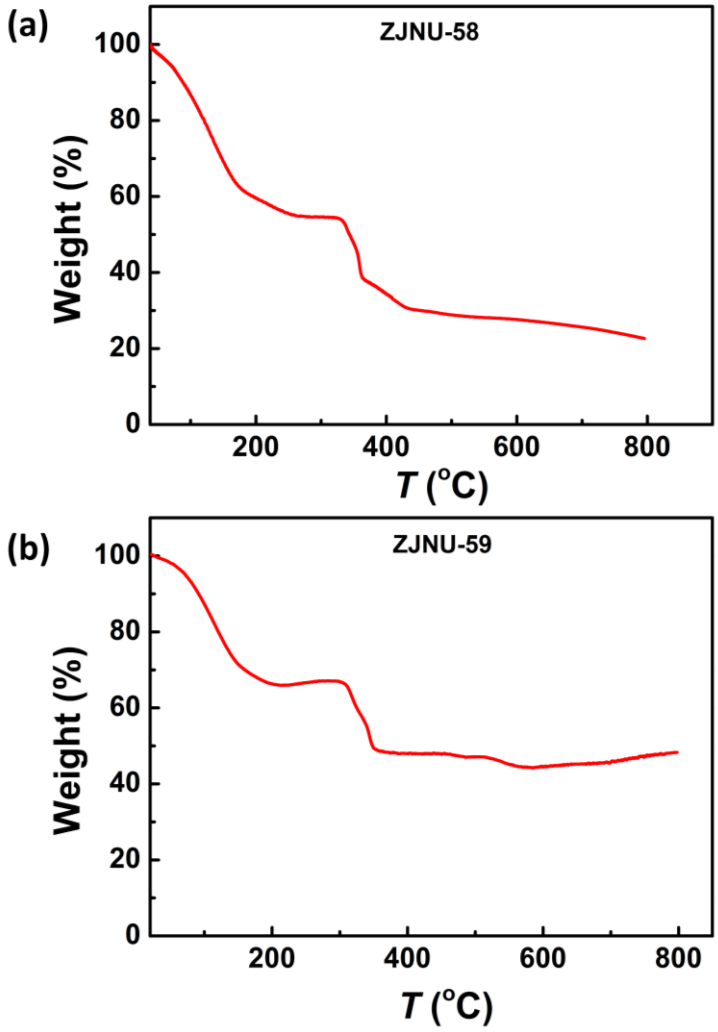

Figure S2. TGA curves of the as-synthesized (a) **ZJNU-58** and (b) **ZJNU-59** under nitrogen atmosphere.

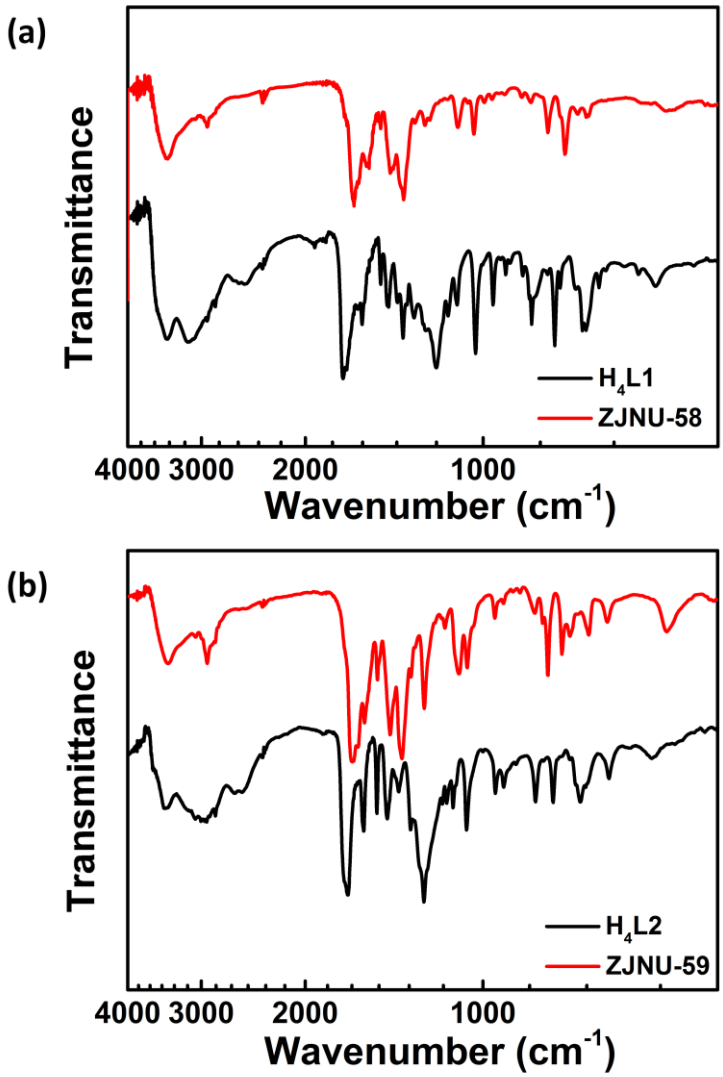

Figure S3. (a) Comparison of FTIR spectra of the organic linker H_4L1 and its corresponding MOF **ZJNU-58**; (b) comparison of FTIR spectra of the organic linker H_4L2 and its corresponding MOF **ZJNU-59**.

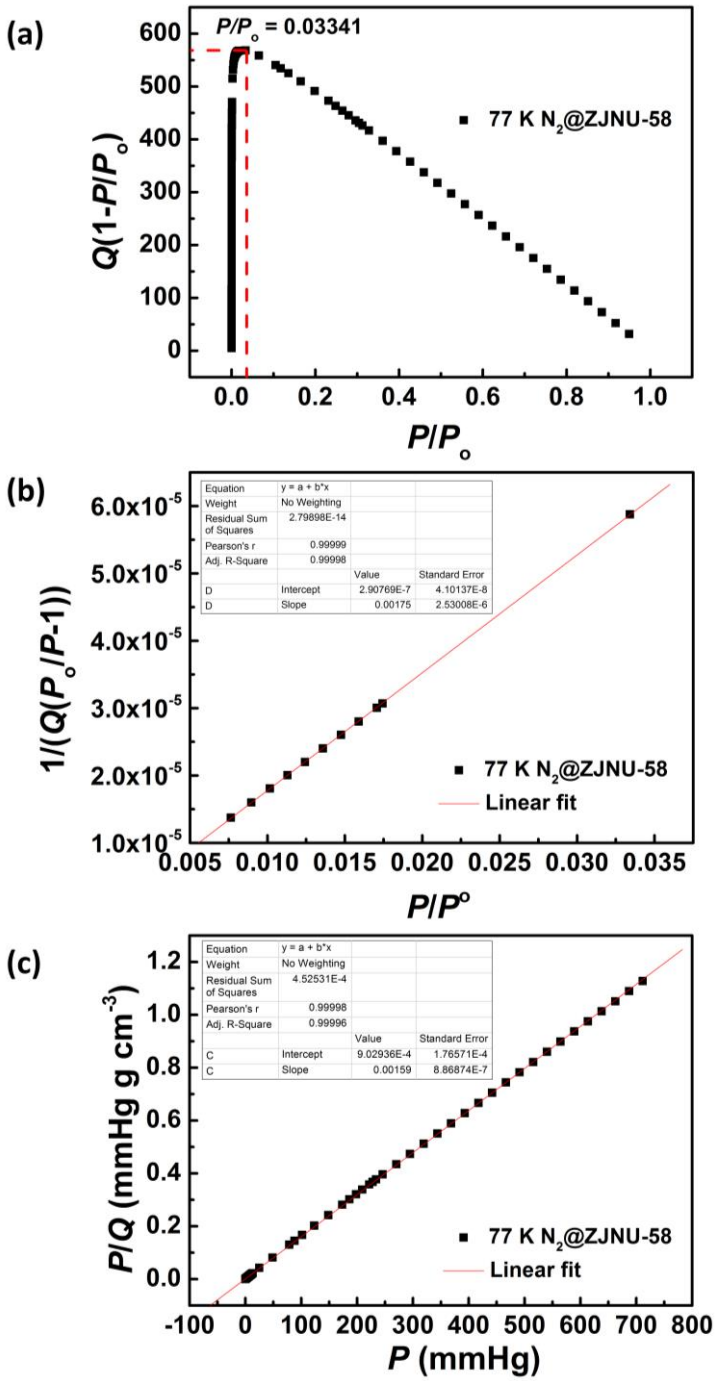

S_{BET} = 1/(2.90769 ×10^{-7} + 0.00175)/22414 × 6.023 × 10^{23} × 0.162 × 10^{-18} = 2487 m^2 g^{-1}

$S_{Langmuir}$ = (1/0.00159)/22414 × 6.023 × 10^{23} × 0.162 × 10^{-18} = 2738 m^2 g^{-1}

BET constant C = 1 + 0.00175/ 2.90769 ×10^{-7} = 6020

$$(P/P_o)_{n_m} = \frac{1}{\sqrt{C}+1} = 0.01272$$

Figure S4. (a) The consistency plot, (b) BET plot and (c) Langmuir plot for **ZJNU-58**.

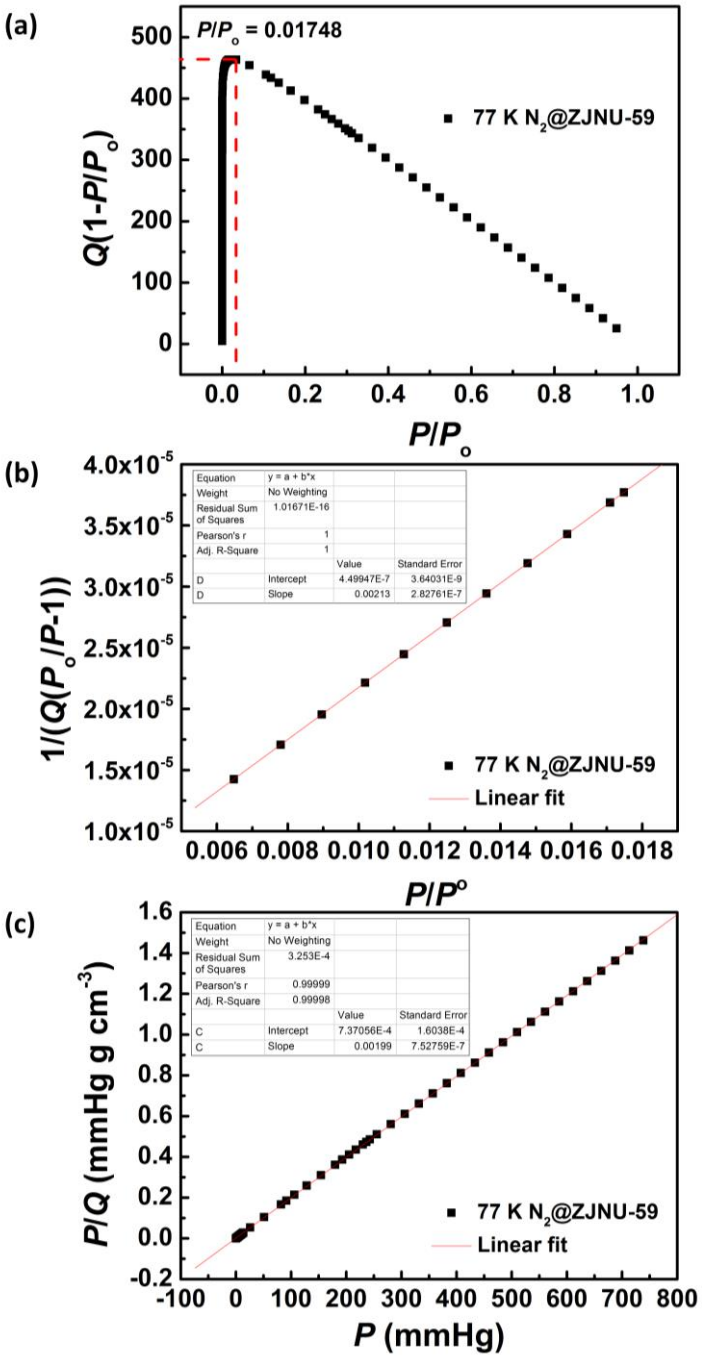

S_{BET} = 1/(4.49947 ×10^{-7} + 0.00213)/22414 × 6.023 × 10^{23} × 0.162 × 10^{-18} = 2043 m^2 g^{-1}

$S_{Langmuir}$ = (1/0.00199)/22414 × 6.023 × 10^{23} × 0.162 × 10^{-18} = 2188 m^2 g^{-1}

BET constant C = 1 + 0.00213/4.49947 ×10^{-7} = 4735

$$(P/P_o)_{n_m} = \frac{1}{\sqrt{C}+1} = 0.01432$$

Figure S5. (a) The consistency plot, (b) BET plot and (c) Langmuir plot for **ZJNU-59**.

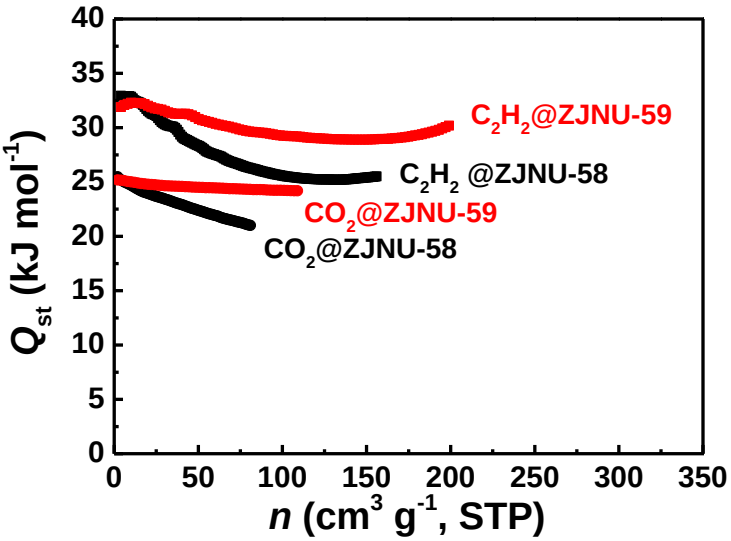

Figure S6. Comparison of the isosteric heats of C_2H_2 and CO_2 adsorption in **ZJNU-58** and **ZJNU-59**.

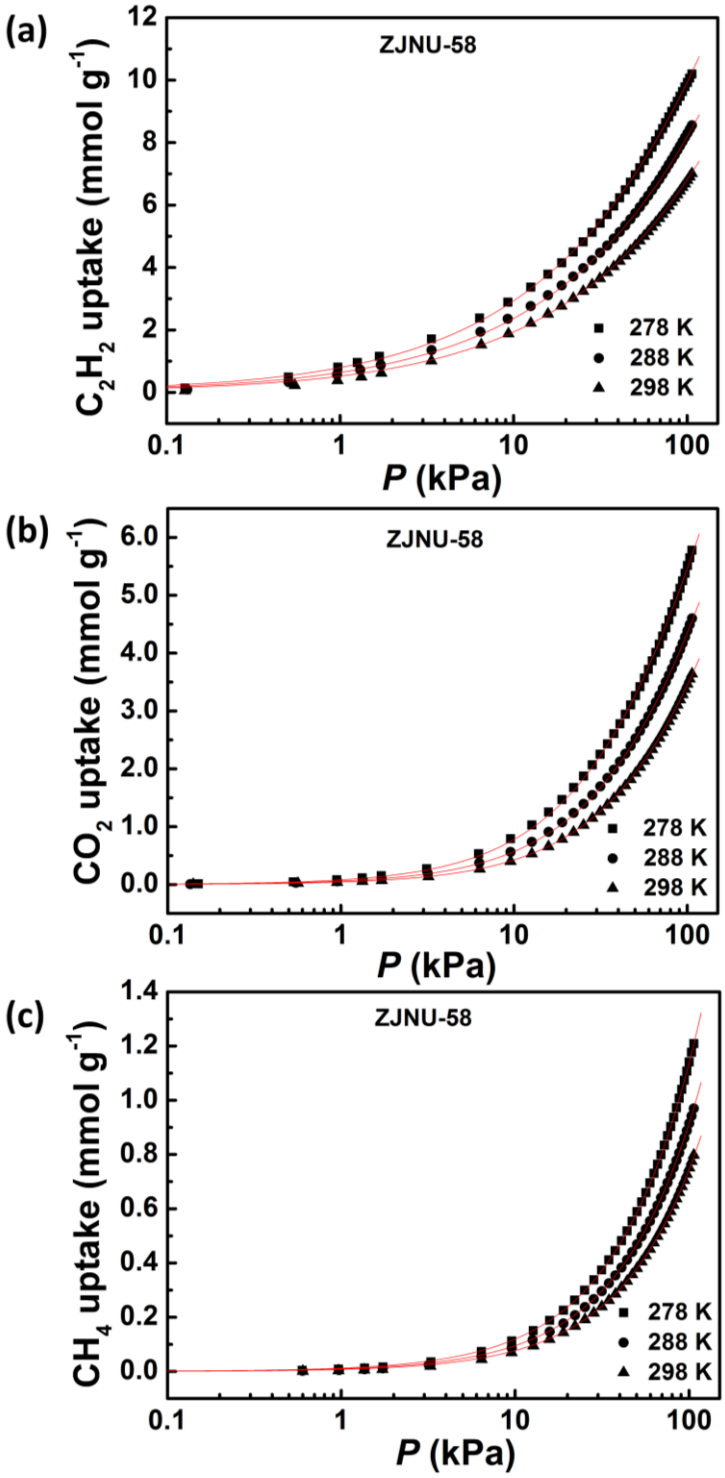

Figure S7. Comparison of the pure-component isotherm data for (a) C_2H_2, (b) CO_2, and (c) CH_4 in **ZJNU-58** with the fitted isotherms (shown by continuous solid lines) at 278 K, 288 K, and 298 K.

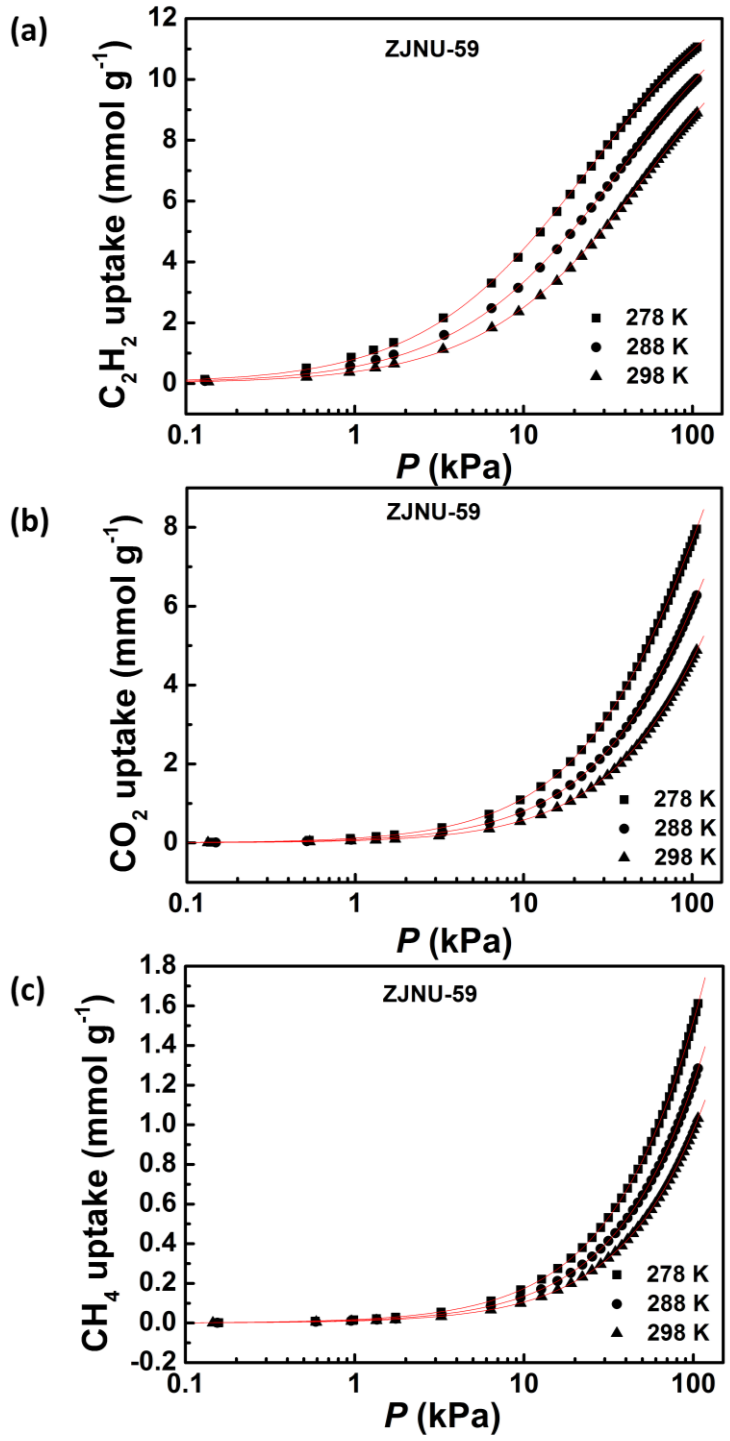

Figure S8. Comparison of the pure-component isotherm data for (a) C_2H_2, (b) CO_2, and (c) CH_4 in **ZJNU-59** with the fitted isotherms (shown by continuous solid lines) at 278 K, 288 K, and 298 K.

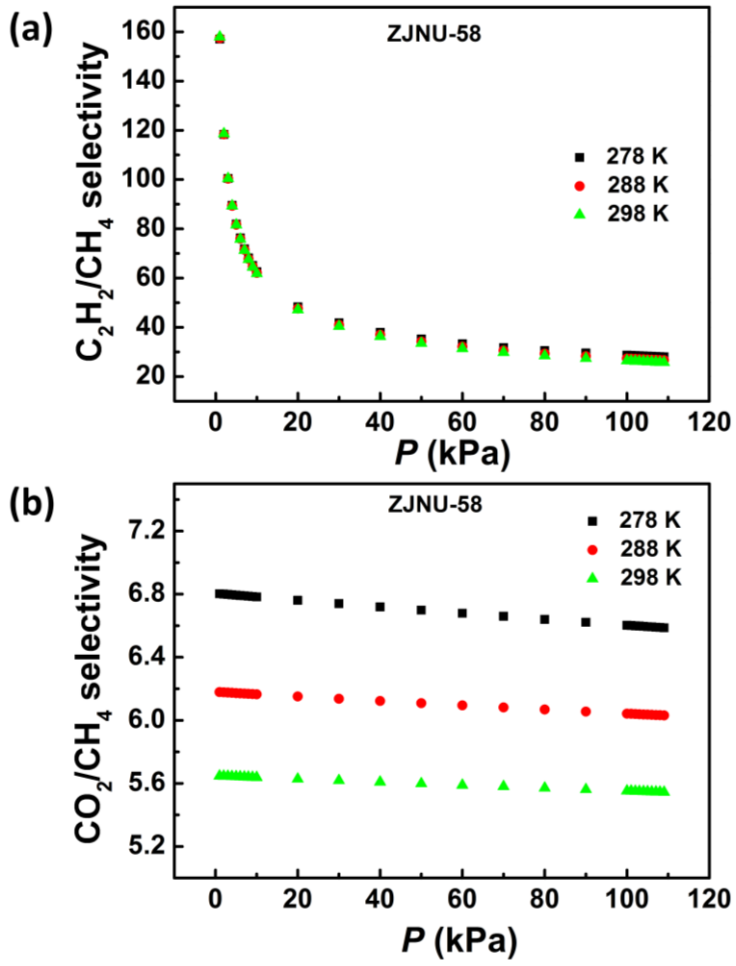

Figure S9. IAST selectivities for the equimolar (a) C_2H_2/CH_4 and (b) CO_2/CH_4 gas mixtures in **ZJNU-58** at three different temperatures of 278 K, 288 K, and 298 K.

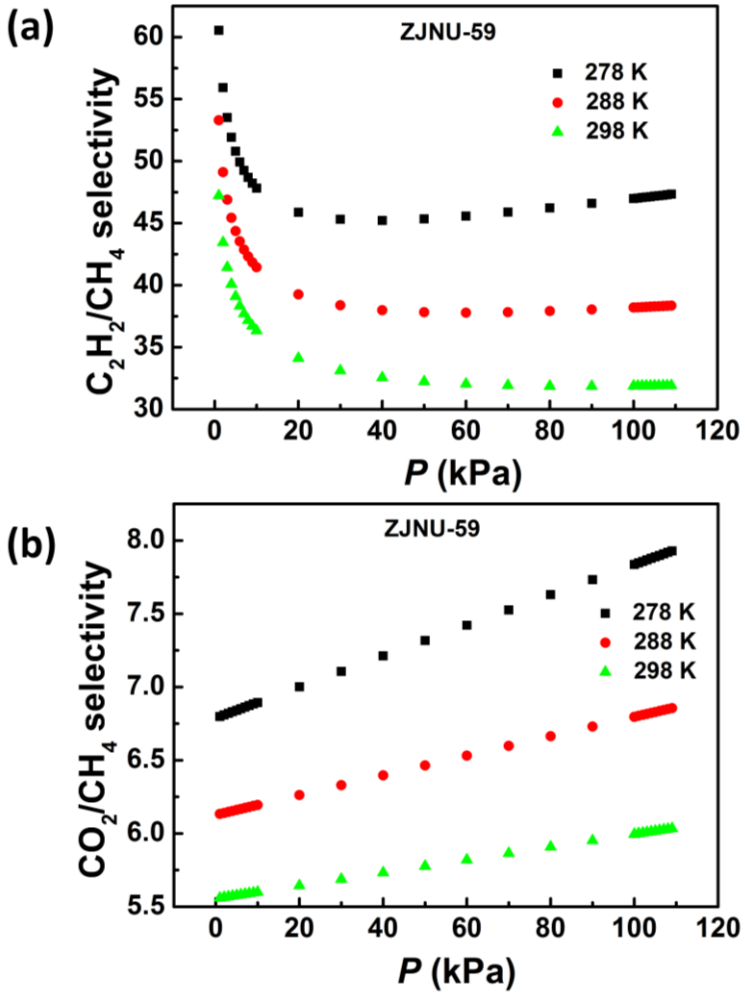

Figure S10. IAST selectivities for the equimolar (a) C_2H_2/CH_4 and (b) CO_2/CH_4 gas mixtures in **ZJNU-59** at three different temperatures of 278 K, 288 K, and 298 K.

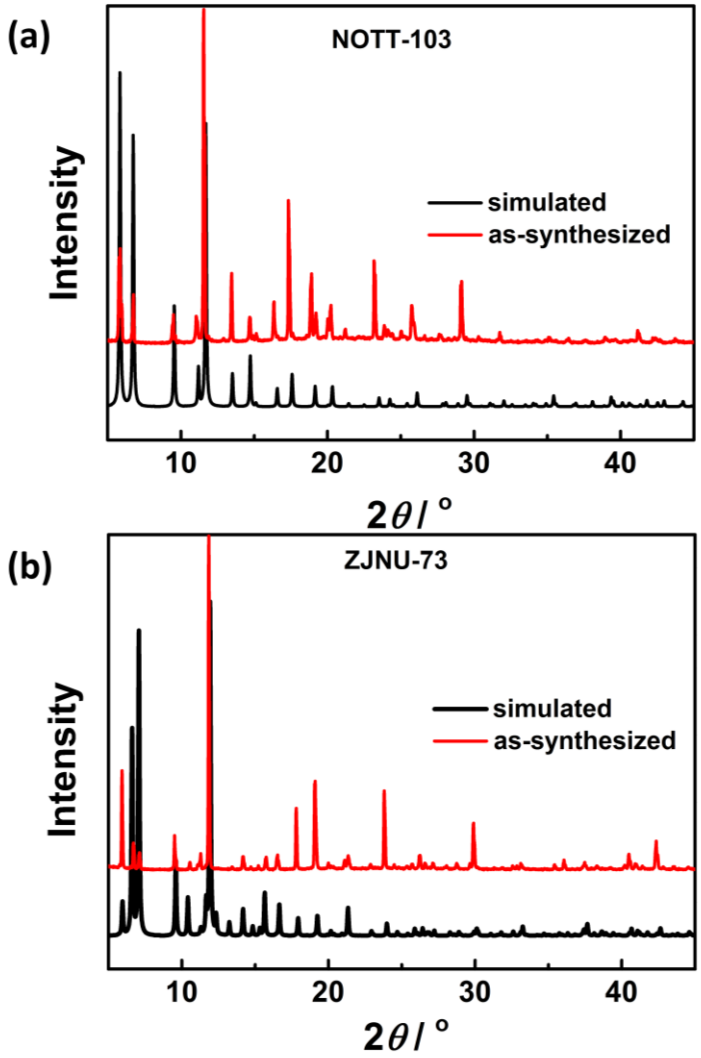

Figure S11. Comparison of the experimental (red) and simulated (black) PXRD patterns for (a) **NOTT-103** and (b) **ZJNU-73**. Note that **NOTT-103** and **ZJNU-73** are the parent MOF compounds for **ZJNU-58** and **ZJNU-59**, respectively.

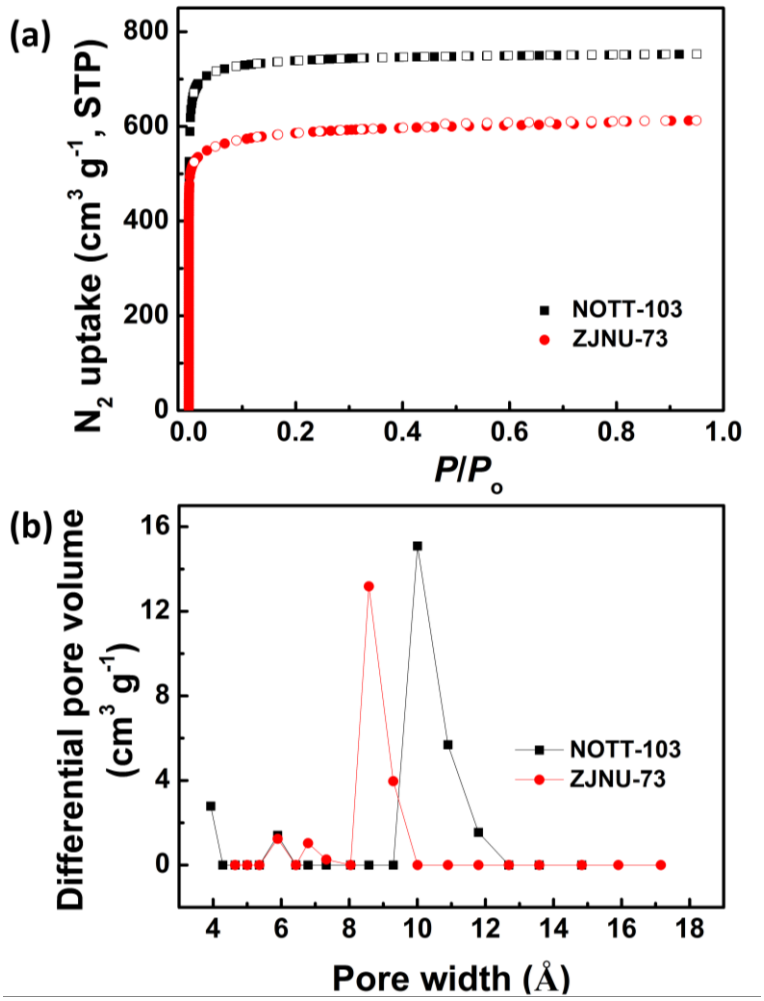

Figure S12. (a) N_2 adsorption-desorption isotherms at 77 K and (b) pore size distributions (calculated by DFT method) of **NOTT-103** and **ZJNU-73**. The solid and open symbols represent adsorption and desorption, respectively. STP = standard temperature and pressure.

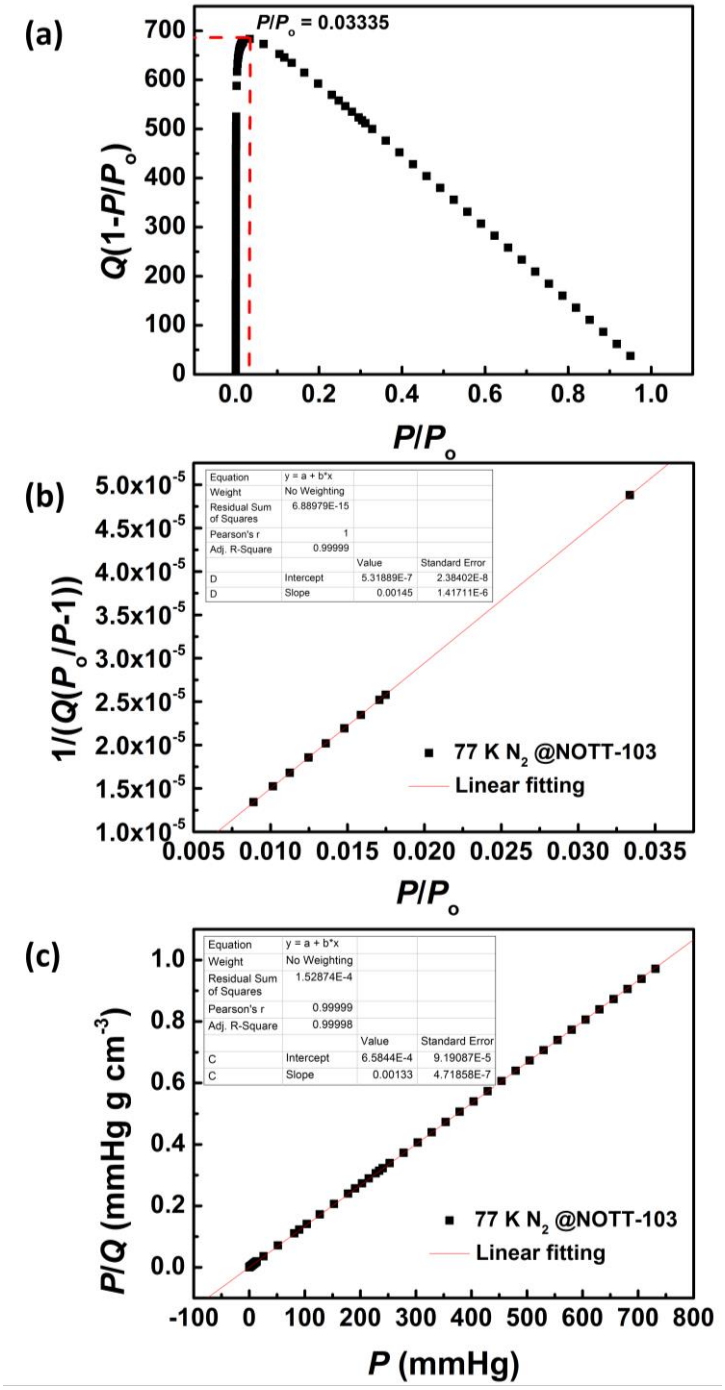

S_{BET} = 1/(5.31889 ×10^{-7}+ 0.00145)/22414 × 6.023 × 10^{23} × 0.162 × 10^{-18} = 3001 m^2 g^{-1}

$S_{Langmuir}$ = (1/0.00133)/22414 × 6.023 × 10^{23} × 0.162 × 10^{-18} = 3273 m^2 g^{-1}

BET constant C = 1 + 0.00145/5.31889 ×10^{-7} = 2727

$$(P/P_o)_{n_m} = \frac{1}{\sqrt{C}+1} = 0.01879$$

Figure S13. (a) The consistency plot, (b) BET plot and (c) Langmuir plot for **NOTT-103**.

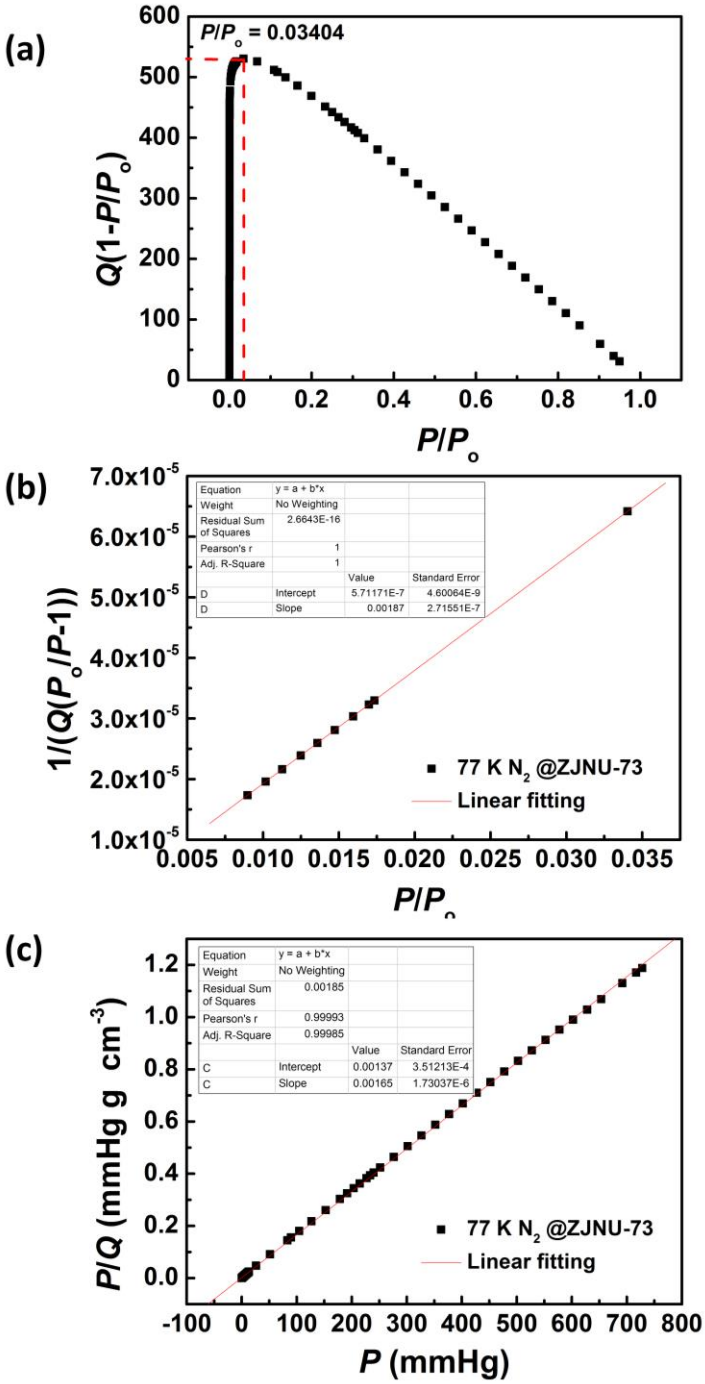

S_{BET} = 1/(5.71171 ×10^{-7}+0.00187)/22414 × 6.023 × 10^{23} × 0.162 × 10^{-18} = 2327 m^2 g^{-1}

$S_{Langmuir}$ = (1/0.00165)/22414 × 6.023 × 10^{23} × 0.162 × 10^{-18} = 2638 m^2 g^{-1}

BET constant C = 1 + 0.00187/5.71171 ×10^{-7} = 3275

$$(P/P_o)_{n_m} = \frac{1}{\sqrt{C}+1} = 0.01717$$

Figure S14. (a) The consistency plot, (b) BET plot and (c) Langmuir plot for **ZJNU-73**.

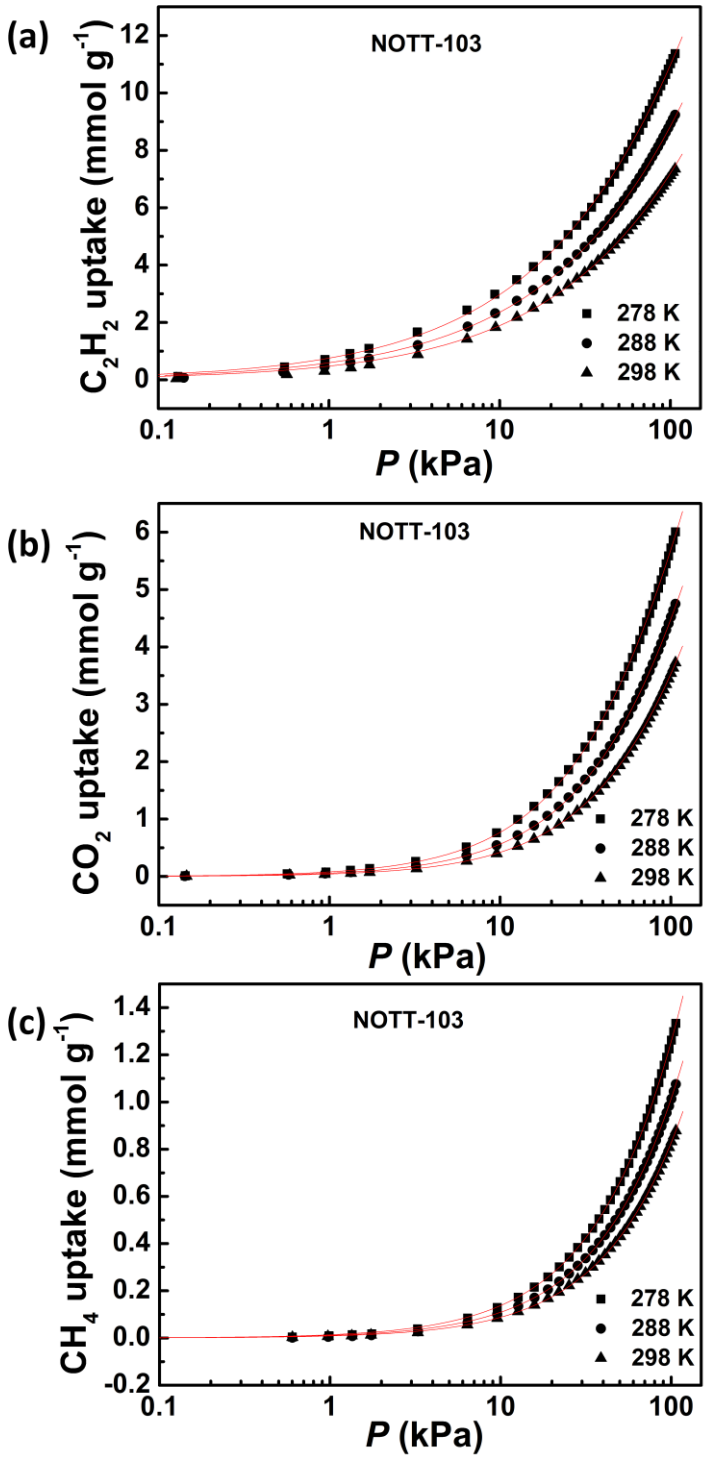

Figure S15. Comparison of the pure-component isotherm data for (a) C_2H_2, (b) CO_2, and (c) CH_4 in **NOTT-103** with the fitted isotherms (shown by continuous solid lines) at 278 K, 288 K, and 298 K.

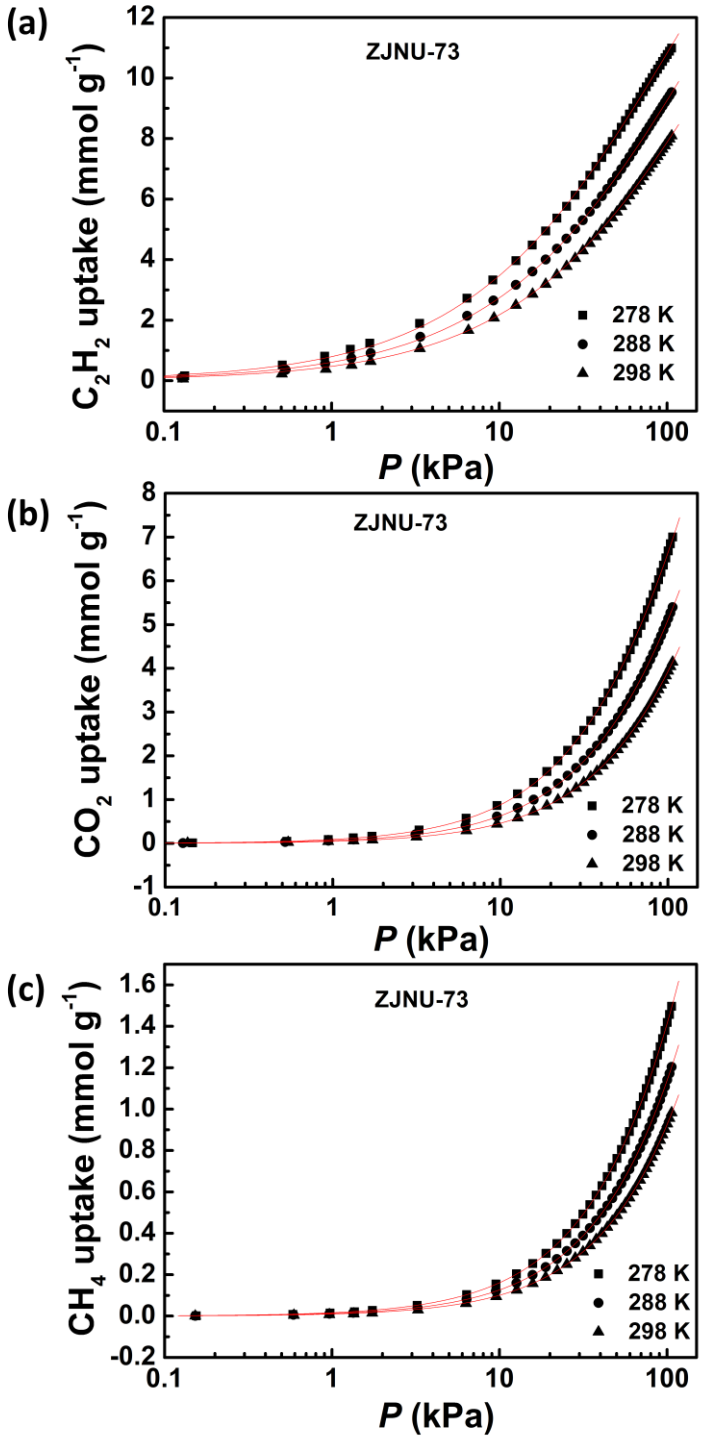

Figure S16. Comparison of the pure-component isotherm data for (a) C_2H_2, (b) CO_2, and (c) CH_4 in **ZJNU-73** with the fitted isotherms (shown by continuous solid lines) at 278 K, 288 K, and 298 K.

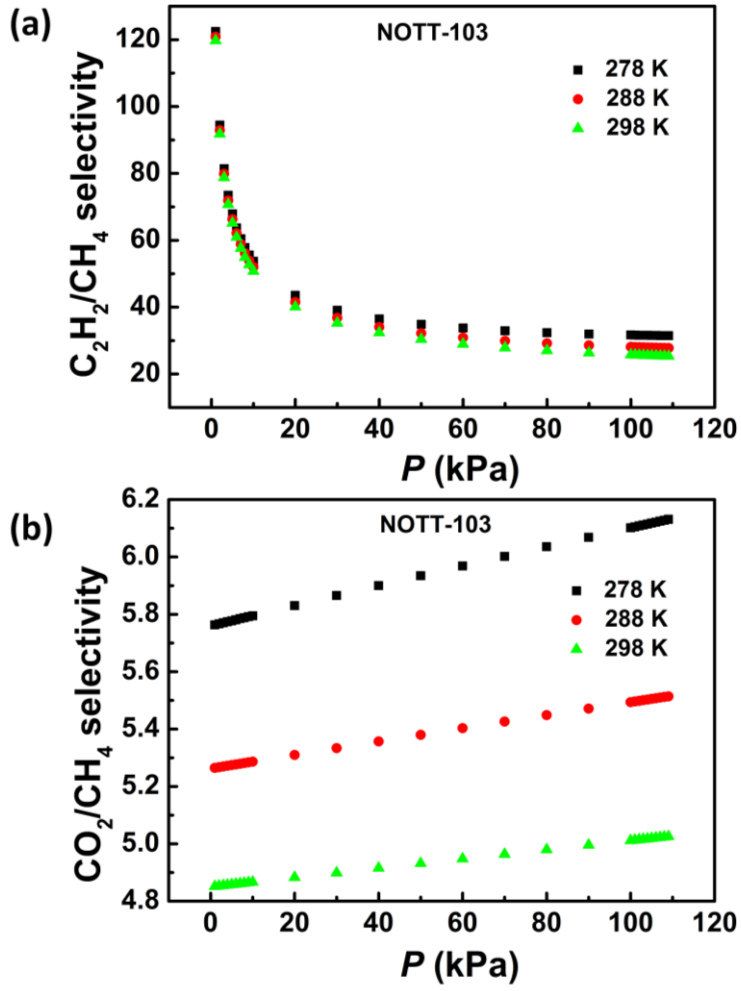

Figure S17. IAST selectivities for the equimolar (a) C_2H_2/CH_4 and (b) CO_2/CH_4 gas mixtures in **NOTT-103** at three different temperatures of 278 K, 288 K, and 298 K.

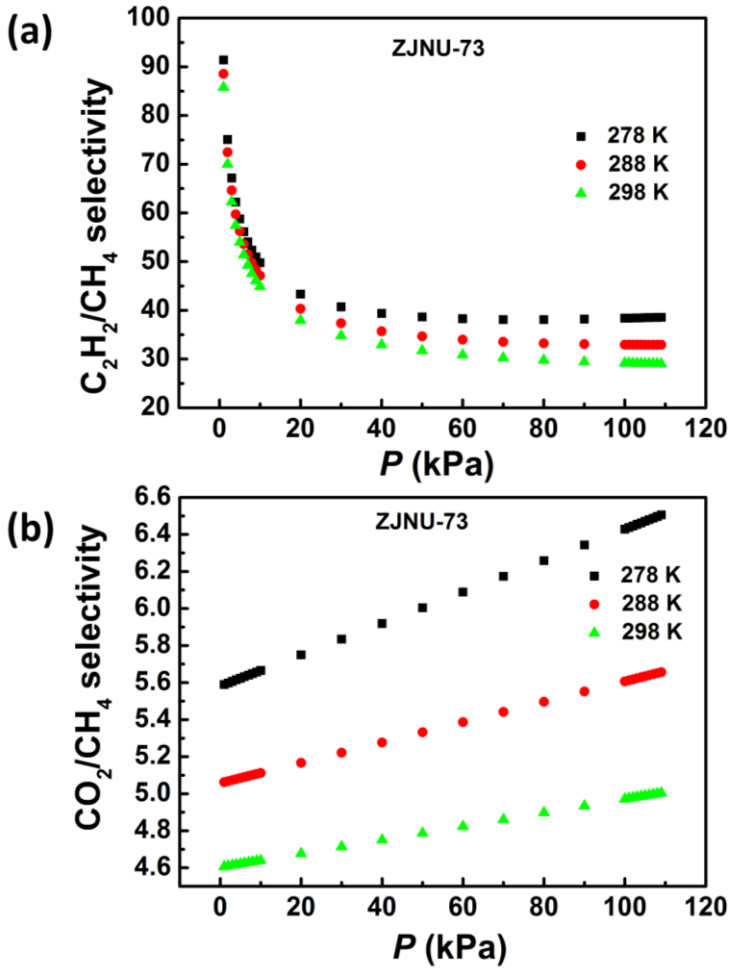

Figure S18. IAST selectivities for the equimolar (a) C_2H_2/CH_4 and (b) CO_2/CH_4 gas mixtures in **ZJNU-73** at three different temperatures of 278 K, 288 K, and 298 K.

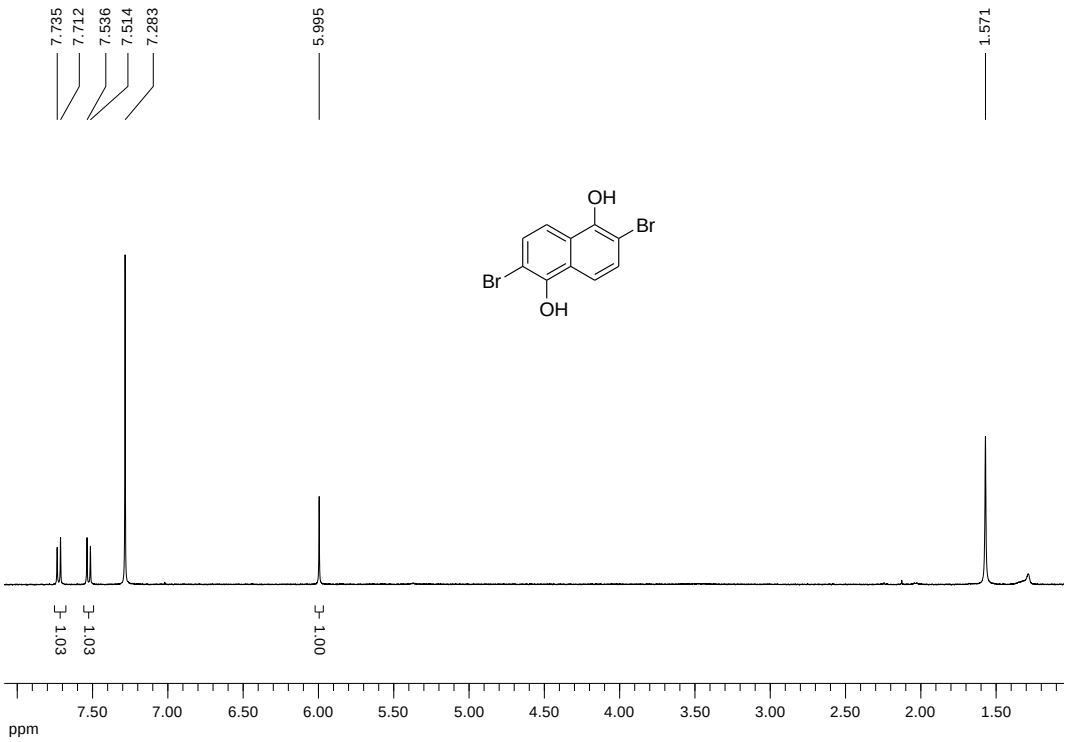
7.735
7.712
7.536
7.514
7.283
5.995
1.571
OH
Br
Br
OH
1.03
1.03
1.00
7.50
7.00
6.50
6.00
5.50
5.00
4.50
4.00
3.50
3.00
2.50
2.00
1.50
ppm

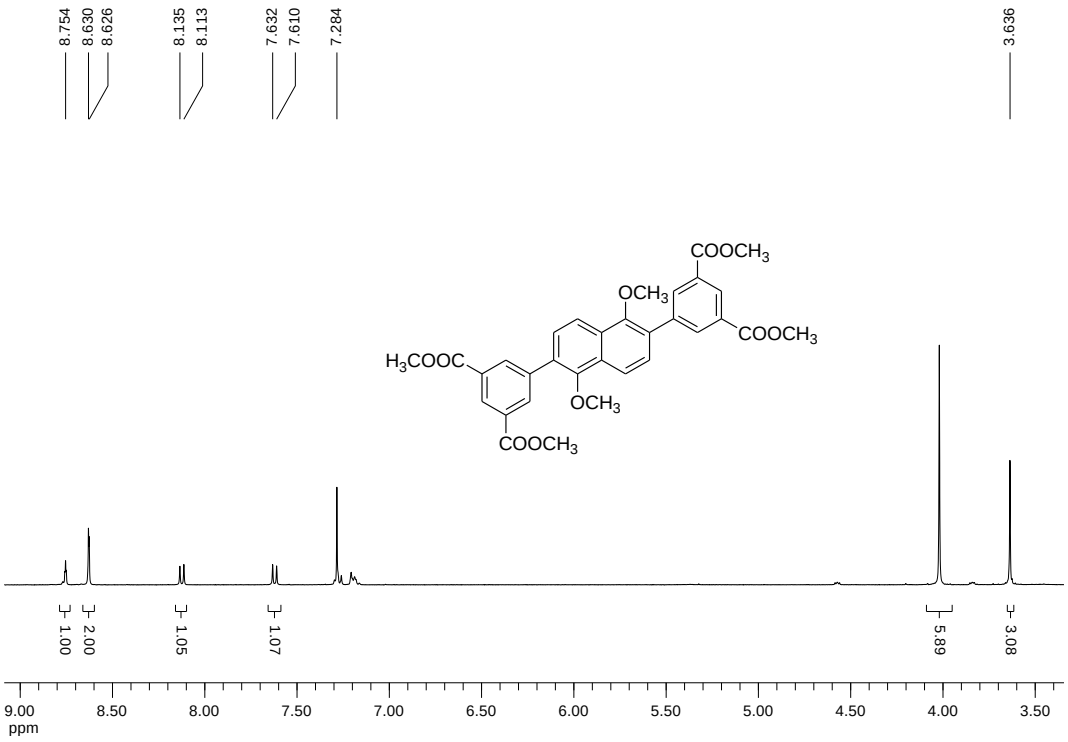
8.754
8.630
8.626
8.135
8.113
7.632
7.610
7.284
3.636
COOCH3
OCH3
COOCH3
H3COOC
OCH3
COOCH3
1.00
2.00
1.05
1.07
5.89
3.08
9.00
8.50
8.00
7.50
7.00
6.50
6.00
5.50
5.00
4.50
4.00
3.50
ppm

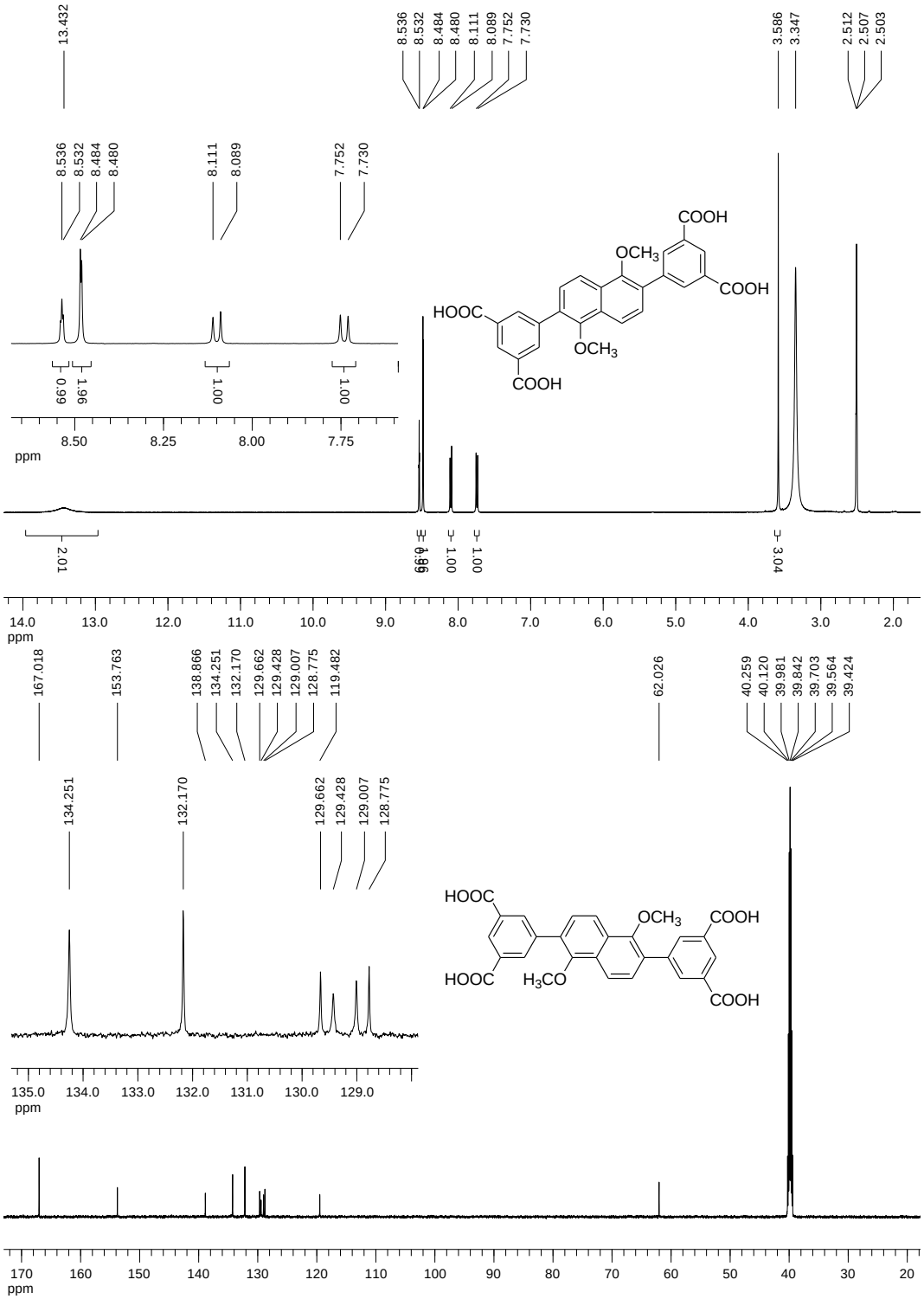
13.432
8.536
8.532
8.484
8.480
8.111
8.089
7.752
7.730
3.586
3.347
2.512
2.507
2.503
COOH
OCH3
COOH
HOOC
OCH3
COOH
2.01
0.99
1.96
1.00
1.00
1.00
1.00
3.04
ppm
167.018
153.763
138.866
134.251
132.170
129.662
129.428
129.007
128.775
119.482
62.026
40.259
40.120
39.981
39.842
39.703
39.564
39.424
HOOC
OCH3
COOH
HOOC
H3CO
COOH
ppm

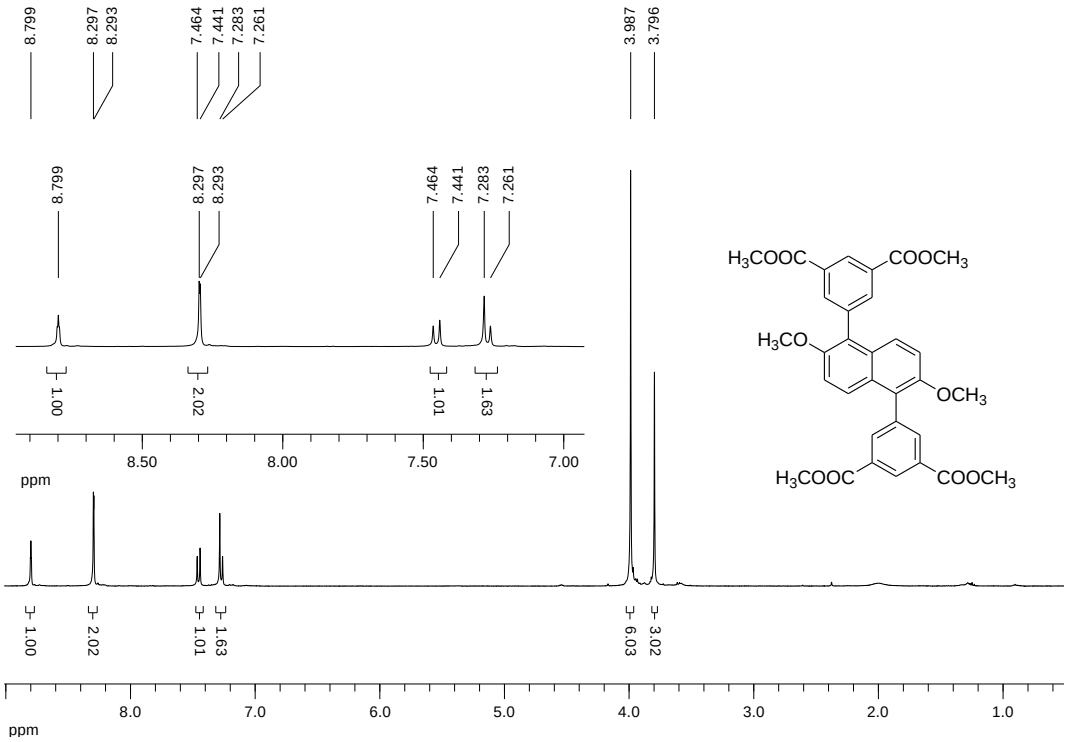
8.799
8.297
8.293
7.464
7.441
7.283
7.261
3.987
3.796
H3COOC
COOCH3
H3CO
OCH3
H3COOC
COOCH3
1.00
2.02
1.01
1.63
6.03
3.02
ppm

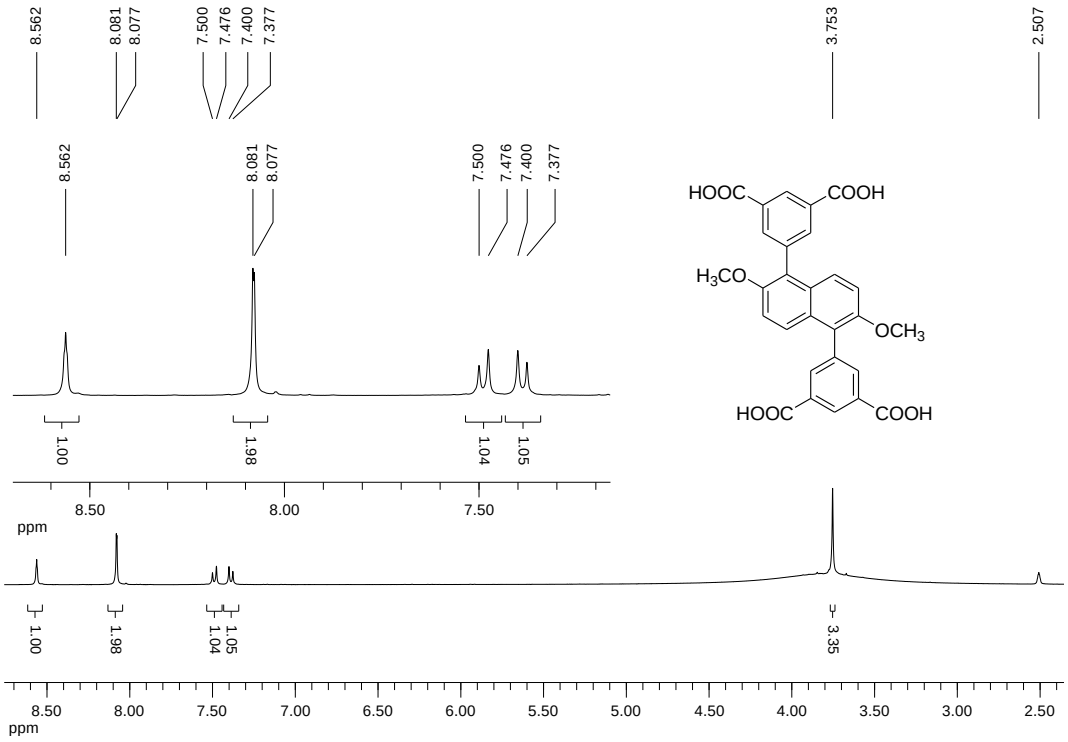
8.562
8.081
8.077
7.500
7.476
7.400
7.377
3.753
2.507
HOOC
COOH
H3CO
OCH3
HOOC
COOH
1.00
1.98
1.04
1.05
3.35
ppm

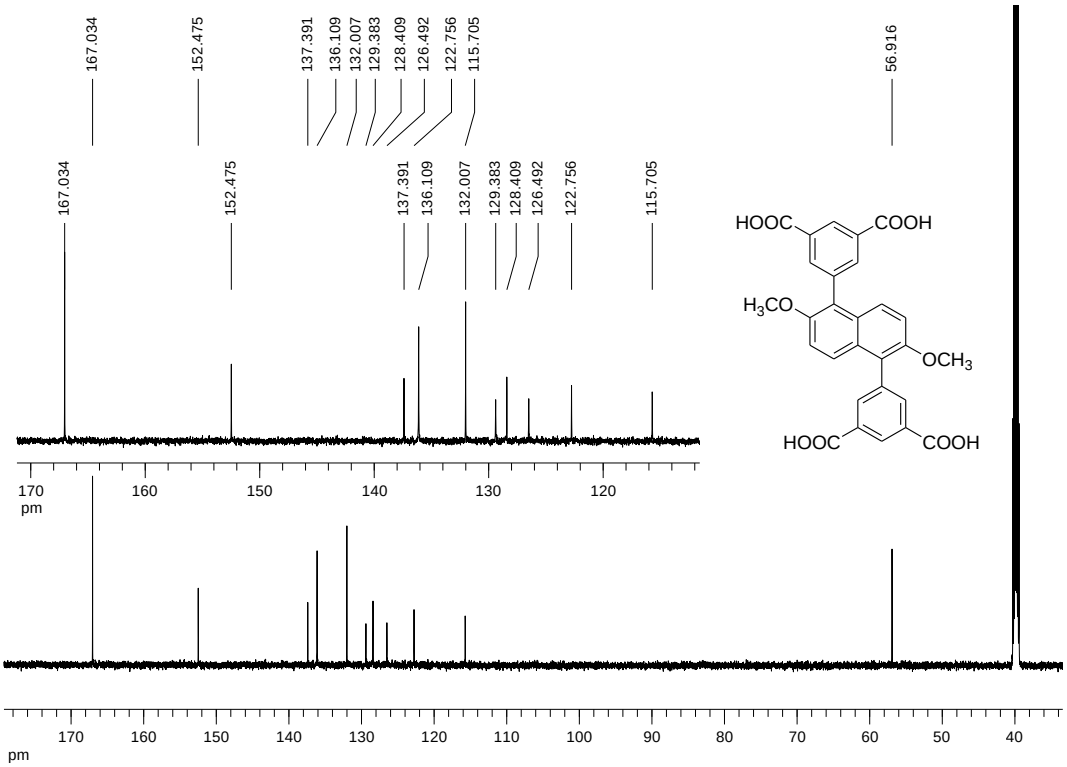

Figure S19. ^{1}H and ^{13}C NMR spectra.

Table S1. Crystal data and structure refinement for **ZJNU-58** and **ZJNU-59**.

MOFs	**ZJNU-58**	**ZJNU-59**
Empirical formula	$C_{84}H_{60}O_{36}Cu_6$	$C_{28}H_{20}O_{12}Cu_2$
Formula weight	2026.56	675.54
λ (Å)	0.71073	0.71073
Crystal system	Monoclinic	Trigonal
Space group	*C*2/c	*R*-3m
Unit cell dimensions	a = 32.3534(9) Å b = 18.2884(4) Å c = 32.7902(11) Å α = 90 ° β = 111.698(4)° γ = 90°	a = 18.6707(9) Å b = 18.6707(9) Å c = 39.262(6) Å α = 90 ° β = 90° γ = 120°
V (Å^3)	18027.0(9)	11853(2)
Z	4	9
D_c (g cm^{-3})	0.747	0.852
μ (mm^{-1})	0.738	0.842
F(000)	4104	3077
Crystal size (mm)	0.28 ×0.18 ×0.16	0.14 x 0.13 x 0.13
θ range for data collection (°)	1.51 to 26.29	2.43 to 21.98
Limiting indices	$-38 \le h \le 39$ $-11 \le k \le 22$ $-40 \le l \le 38$	$-18 \le h \le 18$ $-19 \le k \le 19$ $-41 \le l \le 41$
Reflections collected / unique	51807 / 17901	17305 / 1795
R_{int}	0.0520	0.0832
Max. and min. transmission	0.8911 and 0.8200	0.8985 and 0.8913
Refinement method	Full-matrix least-squares on F^2	Full-matrix least-squares on F^2
Data/restraints/parameters	17901 / 0 / 566	1795 / 0 / 91
Goodness-of-fit on F^2	1.074	1.603
Final R indices [$I > 2\sigma(I)$]	R_1 = 0.1006 wR_2 = 0.2941	R_1 = 0.0861 wR_2 = 0.2342
R indices (all data)	R_1 = 0.1248 wR_2 = 0.3240	R_1 = 0.1159 wR_2 = 0.2430
Largest diff. peak and hole (e·Å^{-3})	1.980 and -0.840	1.040 and -0.477
CCDC	1823336	1823337

Table S2. Langmuir-Freundlich parameters for adsorption of C_2H_2, CO_2, and CH_4 in **ZJNU-58**.

Guest	q_{sat} (mmol g^{-1})	b_0 $(kPa)^{-v}$	E (kJ mol^{-1})	v
C_2H_2	67.19466	1.95659×10^{-5}	14.84	0.58025
CO_2	16.45493	4.29997×10^{-7}	21.62	1
CH_4	21.39211	7.68708×10^{-7}	15.24	1

Table S3. Langmuir-Freundlich parameters for adsorption of C_2H_2, CO_2, and CH_4 in **ZJNU-59**.

Guest	q_{sat} (mmol g^{-1})	b_0 $(kPa)^{-v}$	E (kJ mol^{-1})	v
C_2H_2	14.19285	8.83696×10^{-7}	25.73	0.87549
CO_2	21.09498	1.596×10^{-7}	24.23	1
CH_4	10.7359	9.06108×10^{-7}	17.35	1

Table S4. Langmuir-Freundlich parameters for adsorption of C_2H_2, CO_2, and CH_4 in **NOTT-103**.

Guest	q_{sat} (mmol g^{-1})	b_0 $(kPa)^{-v}$	E (kJ mol^{-1})	v
C_2H_2	100.81876	7.61113×10^{-6}	15.95	0.60446
CO_2	19.76015	3.84451×10^{-7}	21.41	1
CH_4	12.98553	1.25291×10^{-6}	15.60	1

Table S5. Langmuir-Freundlich parameters for adsorption of C_2H_2, CO_2, and CH_4 in **ZJNU-73**.

Guest	q_{sat} (mmol g^{-1})	b_0 $(kPa)^{-v}$	E (kJ mol^{-1})	v
C_2H_2	23.25514	1.31458×10^{-5}	18.26	0.69516
CO_2	24.35673	1.80726×10^{-7}	22.97	1
CH_4	10.29271	1.30584×10^{-6}	16.42	1

Table S6. A summary of pore textural properties and gas adsorption properties of **ZJNU-58**, **ZJNU-59**, NOTT-103 and ZJNU-73.

MOFs	S_{BET} ($m^2 g^{-1}$)	V_p ($cm^3 g^{-1}$)	D_c ($g\ cm^{-3}$)	C_2H_2 uptake at 1 atm [cm^3 (STP) g^{-1}]			CO_2 uptake at 1 atm [cm^3 (STP) g^{-1}]			CH_4 uptake at 1 atm [cm^3 (STP) g^{-1}]		
				278 K	288 K	298 K	278 K	288 K	298 K	278 K	288 K	298 K
ZJNU-58	2487	0.9758	0.7068	228.5	191.7	157.1	129.5	103.1	81.6	27.1	21.7	17.9
ZJNU-59	2043	0.7810	0.8062	248.1	224.7	199.5	178.3	140.6	109.4	36.1	28.8	23.1
NOTT-103	3001	1.1645	0.6432	254.9	207.0	164.8	134.6	106.5	83.5	29.9	24.1	19.7
ZJNU-73	2327	0.9476	0.7307	246.3	213.6	181.4	156.9	121.0	92.9	33.5	27.0	22.0

Continued

MOFs	C_2H_2/CH_4 IAST adsorption selectivity at 1 atm			CO_2/CH_4 IAST adsorption selectivity at 1 atm		
	278 K	288 K	298 K	278 K	288 K	298 K
ZJNU-58	28.0	26.7	25.7	6.59	6.03	5.54
ZJNU-59	47.3	38.4	31.9	7.93	6.86	6.03
NOTT-103	31.5	27.8	25.3	6.13	5.51	5.03
ZJNU-73	38.6	32.9	29.0	6.51	5.66	5.00

S_{BET}: BET specific surface area; V_p: pore volume; D_c: framework density

References

(1) Jiao, J.; Dou, L.; Liu, H.; Chen, F.; Bai, D.; Feng, Y.; Xiong, S.; Chen, D.-L.; He, Y., An aminopyrimidine-functionalized cage-based metal-organic framework exhibiting highly selective adsorption of C_2H_2 and CO_2 over CH_4. *Dalton Trans.* **2016**, *45*, 13373-13382.

(2) Krishna, R. The maxwell-stefan description of mixture diffusion in nanoporous crystalline materials. *Microporous Mesoporous Mater.* **2014**, *185*, 30-50.

(3) Krishna, R. Methodologies for evaluation of metal-organic frameworks in separation applications. *RSC Adv.* **2015**, *5*, 52269-52295.

(4) Krishna, R. Screening metal-organic frameworks for mixture separations in fixed-bed adsorbers using a combined selectivity/capacity metric. *RSC Adv.* **2017**, *7*, 35724-35737.

(5) Krishna, R. Methodologies for screening and selection of crystalline microporous materials in mixture separations. *Sep. Purif. Technol.* **2018**, *194*, 281-300.